

The effect of variations in the input physics on the cosmic distribution of metals predicted by simulations

Robert P. C. Wiersma,^{1,2*} Joop Schaye,² and Tom Theuns^{3,4}

¹*Max-Planck-Institut für Astrophysik, Karl-Schwarzschild-Strasse 1, D-85478 Garching, Germany*

²*Leiden Observatory, Leiden University, P.O. Box 9513, 2300 RA Leiden, the Netherlands*

³*Institute for Computational Cosmology, Department of Physics, University of Durham, South Road, Durham, DH1 3LE, UK*

⁴*Department of Physics, University of Antwerp, Groenenborgerlaan 171, B-2020 Antwerpen, Belgium*

16 November 2021

ABSTRACT

We investigate how a range of physical processes affect the cosmic metal distribution using a suite of cosmological, hydrodynamical simulations. Focusing on redshifts $z = 0$ and 2 , we study the metallicities and metal mass fractions for stars as well as for the interstellar medium (ISM), and several more diffuse gas phases. We vary the cooling rates, star formation law, structure of the ISM, properties of galactic winds, feedback from AGN, supernova type Ia time delays, reionization, stellar initial mass function, and cosmology. In all models stars and the warm-hot intergalactic medium (WHIM) constitute the dominant repository of metals, while for $z \gtrsim 2$ the ISM is also important. In models with galactic winds, predictions for the metallicities of the various phases vary at the factor of two level and are broadly consistent with observations. The exception is the cold-warm intergalactic medium (IGM), whose metallicity varies at the order of magnitude level if the prescription for galactic winds is varied, even for a fixed wind energy per unit stellar mass formed, and falls far below the observed values if winds are not included. At the other extreme, the metallicity of the intra-cluster medium (ICM) is largely insensitive to the presence of galactic winds, indicating that its enrichment is regulated by other processes. The mean metallicities of stars ($\sim Z_{\odot}$), the ICM ($\sim 10^{-1} Z_{\odot}$), and the WHIM ($\sim 10^{-1} Z_{\odot}$) evolve only slowly, while those of the cold halo gas and the IGM increase by more than an order of magnitude from $z = 5$ to 0 . Higher velocity outflows are more efficient at transporting metals to low densities, but actually predict lower metallicities for the cold-warm IGM since the winds shock-heat the gas to high temperatures, thereby increasing the fraction of the metals residing in, but not the metallicity of, the WHIM. Besides galactic winds driven by feedback from star formation, the metal distribution is most sensitive to the inclusion of metal-line cooling and feedback from AGN. We conclude that observations of the metallicity of the low-density IGM have the potential to constrain the poorly understood feedback processes that are central to current models of the formation and evolution of galaxies.

Key words: cosmology: theory — galaxies: formation — galaxies: abundances — intergalactic medium

1 INTRODUCTION

The spatial distribution of elements synthesised in stars (henceforth ‘metals’) provides an archaeological record of past star formation activity and of the various energetic phenomena that stirred and mixed these metals. Recent cosmological simulations of galaxy formation follow the different stellar evolutionary channels through which metals are produced, and include some processes that cause metals to escape from their parent galaxy. Here we will investigate to what extent these simulations produce realistic enrichment pat-

terns, which physical processes affect the metal distribution, and how robust the predictions are.

Observations can constrain integrated stellar and nebular (ISM) abundances of galaxies (for $z \lesssim 1$ see e.g. Kobulnicky & Zaritsky 1999; Kunth & Östlin 2000; Tremonti et al. 2004; Dunne et al. 2003, for $z \approx 1$ see Churchill et al. 2007, for $z \gtrsim 2$ see Erb et al. 2006; Mannucci et al. 2009). Metals in cold gas can be observed in absorption against a background source, see the damped Lyman-alpha observations at $z \approx 3$ (e.g. Pettini et al. 1994; Prochaska et al. 2003) and at lower (e.g. Meiring et al. 2009) and higher redshift (e.g. Ando et al. 2007; Price et al. 2007). If the background source is sufficiently bright, then this technique

* E-mail: wiersma@mpa-garching.mpg.de

can also be applied to more diffuse gas (e.g. Songaila & Cowie 1996; Cowie & Songaila 1998; Ellison et al. 2000; Schaye et al. 2000, 2003, 2007; Simcoe et al. 2004; Scannapieco et al. 2006; Aguirre et al. 2008). The metallicity of the ICM is inferred from X-ray observations (e.g. Mushotzky et al. 1996; de Plaa et al. 2006; Sato et al. 2007; Rasmussen & Ponman 2007; Maughan et al. 2008; Leccardi & Molendi 2008; Snowden et al. 2008).

These observations use different tools to observe a variety of elements in a variety of ionization states, and it is not always obvious how to convert all these measurements to a common ‘metallicity’. Often this is done assuming that the relative abundances of elements equal those measured in the Sun. Unfortunately even the assumed metallicity of the Sun itself varies between authors. Here we assume $Z_{\odot} = 0.0127$, and solar abundances from the default settings of CLOUDY (version 07.02, last described by Ferland et al. 1998).

Convolving metallicity with the fraction of baryonic mass in each of the different phases then yields a census of cosmic metals (e.g. Fukugita et al. 1998). It must, however, be kept in mind that a large fraction of the metals are potentially not accounted for by the current data. For example, a large portion of $z = 0$ baryons are thought to reside in the warm-hot intergalactic medium (WHIM), which has not yet been convincingly detected. If, as is likely, the WHIM is also metal enriched, then it could harbour a significant amount of metals. Similarly, the prevalence of hot ($T \gtrsim 10^5$ K) metals at $z \gtrsim 2$ is currently poorly constrained. Gas cooling, star formation, galaxy interactions, ram pressure stripping, stellar and galactic winds all cause gas and hence metals to be cycled between the different phases, which makes it complicated to relate the observed metal distribution to the original source and/or enrichment process.

A theoretical calculation of the census of cosmic metals must take into account their production by nucleosynthesis, their initial distribution, and the mixing that occurs in later stages. Numerical simulations that include such ‘chemo-dynamics’ have become increasingly sophisticated since the early work by Theis et al. (1992), usually concentrating on the evolution of a single galaxy (Steinmetz & Muller 1995; Raiteri et al. 1996; Berczik 1999; Recchi et al. 2001; Kawata 2001; Kawata & Gibson 2003; Kobayashi 2004; Mori & Umemura 2006; Stinson et al. 2006; Governato et al. 2007; Bekki & Chiba 2009; Rahimi et al. 2010; Pasetto et al. 2010), or a cluster of galaxies (e.g. Lia et al. 2002; Valdarnini 2003; Tornatore et al. 2004; Sommer-Larsen et al. 2005; Romeo et al. 2006; Tornatore et al. 2007; Fabjan et al. 2010) in a cosmological context. These simulations include interpolation tables from stellar evolution calculations for the production of metals, but implement the enrichment processes explicitly, for example by injecting metal-enriched gas near a site of star formation in a galactic wind. The fluxes of metals between phases due to gas cooling and galaxy/gas interactions are computed explicitly by these hydro-codes. Early simulations that were also used to look at the metals outside galaxies include Cen & Ostriker (1999), Mosconi et al. (2001) and Theuns et al. (2002). Subsequent authors implemented more physics while increasing resolution and/or box size in order to minimise numerical effects (e.g. Scannapieco et al. 2005; Oppenheimer & Davé 2006; Cen & Ostriker 2006; Brook et al. 2007; Kobayashi et al. 2007; Oppenheimer & Davé 2008; Wiersma et al. 2009, 2010; Shen et al. 2009; Tornatore et al. 2009).

In this paper we use cosmological hydrodynamical simulations of the formation of galaxies to attempt to answer the question ‘Where are the metals?’, by computing the evolution of the frac-

tion of metals in stars and various gas phases. Our suite of numerical simulations (the OWLS suite; Schaye et al. 2010), includes runs that differ in terms of their resolution, input physics, and numerical implementation of physical processes. We use it to investigate what physical processes are most important, how reliable the predictions are, and to what extent these depend on the sometimes poorly understood physics (see Sommer-Larsen & Fynbo 2008, for a similar investigation). In Wiersma et al. (2009) we introduced the method and described some of the numerical issues involved, but analysed only a single physical model (the OWLS reference model). Here we vary the cooling rates, star formation law, structure of the ISM, properties of galactic winds, feedback from AGN, supernova type Ia time delays, reionization, stellar initial mass function, and cosmology.

This paper is organised as follows. Section 2 introduces the simulations used. Those familiar with the OWLS project may skip to the results in Section 3, which begins with an overview before discussing the physical variations which are the most relevant to the metal distribution. This section closes with a summary of all the simulations in the OWLS suite in Section 3.8. In Section 4 we present our conclusions.

2 SIMULATIONS

The OWLS suite (Schaye et al. 2010) consists of more than fifty large, cosmological, gas-dynamical simulations in periodic boxes, performed using the N -body Tree-PM, SPH code GADGET III; see Tables 1 and 2 in Schaye et al. (2010) for a full list of parameters. GADGET III is an updated version of GADGET II (Springel 2005), to which we added new physics modules for star formation (Schaye & Dalla Vecchia 2008), feedback from supernovae (SNe) in the form of galactic winds (Dalla Vecchia & Schaye 2008), feedback from accreting black holes (Booth & Schaye 2009), radiative cooling and heating in the presence of an ionizing background (Wiersma et al. 2009), and stellar evolution (Wiersma et al. 2009). In this simulation suite, numerical and poorly known physical parameters are varied with respect to a ‘reference’ model, to assess which conclusions are robust, and which processes dominate. The cosmological parameters of the reference model, its subgrid and their models and their numerical implementation, are discussed briefly in the next section. GIMIC (Crain et al. 2009) is a complementary suite of simulations performed with the same simulation code, but employs a single set of parameters to investigate how star formation depends on environment, by simulating regions picked from a large volume simulation. Here we give a short overview of the code, concentrating especially on those processes that are directly relevant to metal enrichment.

2.1 The REFERENCE model

The REFERENCE model assumes a cosmologically flat, vacuum energy dominated Λ CDM universe with cosmological parameters $[\Omega_m, \Omega_b, \Omega_\Lambda, \sigma_8, n_s, h] = [0.238, 0.0418, 0.762, 0.74, 0.951, 0.73]$, as determined from the WMAP 3-year data and consistent¹ with the WMAP 5-year data. The assumed primordial helium mass fraction is $Y = X_{\text{He}} = 0.248$. We used CMBFAST (version 4.1; Seljak & Zaldarriaga 1996) to compute the linear power-

¹ Our value of σ_8 is 8 % lower than the best-fit WMAP 7-year data (Jarosik et al. 2010).

spectrum at the starting redshift $z = 127$. Simulations with given box size use identical initial conditions (phases and amplitudes of the Gaussian density field), enabling us to investigate in detail the effects of the imposed physics on the forming galaxies and the intergalactic medium. The simulations are performed with a gravitational softening that is constant in comoving variables down to $z = 2.91$, below which we switch to a softening that is constant in proper units. This is done because we expect two-body scattering to be less important at late times, when haloes contain more particles.

- *Gas cooling and photoionization* Radiative cooling and heating are implemented as described in Wiersma et al. (2009)². In brief, the radiative rates are computed element-by-element, in the presence of an imposed ionizing background and the CMB. We use the redshift-dependent ionizing background due to galaxies and quasars computed by Haardt & Madau (2001, hereafter HM01). Contributions to cooling and heating of eleven elements (hydrogen, helium, carbon, nitrogen, oxygen, neon, magnesium, silicon, sulphur, calcium, and iron) are tabulated as a function of density, temperature and redshift, using the publicly available photo-ionization package CLOUDY, last described by Ferland et al. (1998), assuming the gas to be optically thin and in (photo-)ionization equilibrium.

Hydrogen reionization is implemented by switching on the evolving, uniform ionizing background at redshift $z = 9$. Prior to this redshift the cooling rates are computed using the CMB and a photo-dissociating background which we obtain by cutting off the $z = 9$ HM01 spectrum above 1 Ryd, which suppresses H_2 formation and cooling at all redshifts (we do not resolve haloes in which Pop. III stars that form by H_2 cooling).

- *Star formation* The interstellar medium of the Milky Way consists of multiple ‘phases’: a warm component in which hot super nova bubbles envelope and penetrate cold ‘clouds’. Current cosmological galaxy formation simulations cannot resolve such a multiphase ISM, and in addition not all the physics that governs the interaction between these phases, and the star formation in them, is included. Instead of trying to simulate these physical processes, we use the following ‘sub-grid’ model. ISM gas is assumed to follow a pressure-density relation

$$P = P_0 (n_H / n_{H;\text{thres}})^{\gamma_{\text{eff}}} \quad (1)$$

where $P_0/k = 1.08 \times 10^3 \text{ cm}^{-3} \text{ K}$. We use $\gamma_{\text{eff}} = 4/3$ for which both the Jeans mass and the ratio of the Jeans length to the SPH kernel are independent of the density, thus preventing spurious fragmentation due to a lack of numerical resolution. Finally, only gas dense enough to be gravo-thermally unstable, $n_H \geq n_{H;\text{thres}} = 10^{-1} \text{ cm}^{-3}$, is assumed to be multiphase and star-forming gas (Schaye 2004). It is on this gas that the pressure-density relation (Eq. 1) is imposed.

Star formation in disk galaxies is observed to follow a power-law ‘Kennicutt-Schmidt’ (Kennicutt 1998) relation between the surface density of star formation, $\dot{\Sigma}_*$, and the gas surface density, Σ_g ,

$$\dot{\Sigma}_* = 1.5 \times 10^{-4} \text{ M}_\odot \text{ yr}^{-1} \text{ kpc}^{-2} \left(\frac{\Sigma_g}{1 \text{ M}_\odot \text{ pc}^{-2}} \right)^{1.4}. \quad (2)$$

We have implemented this surface density law as a pressure law. A star formation rate which depends on ISM pressure guarantees that simulated disk galaxies in which the disk is vertically in approximate hydrostatic equilibrium follow the observed

² We used their Eq. (3) rather than (4) and CLOUDY version 05.07 rather than 07.02.

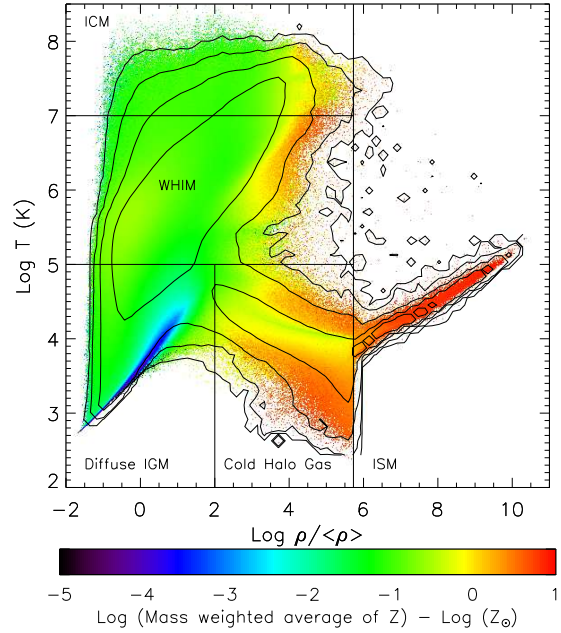


Figure 1. Mass weighted metal distribution in temperature-density space at $z = 0$ in simulation REFERENCE_L100N512. The colour scale gives the metallicity. The contours indicate the metal mass distribution and are logarithmically spaced by 1 dex. The straight lines indicate the adopted division of the gas into: star-forming gas (i.e., $n_H > 0.1 \text{ cm}^{-3}$), diffuse IGM ($\rho < 10^2 \langle \rho \rangle$, $T < 10^5 \text{ K}$), cold halo gas ($\rho > 10^2 \langle \rho \rangle$, $T < 10^5 \text{ K}$), WHIM ($10^5 \text{ K} < T < 10^7 \text{ K}$), and ICM ($T > 10^7 \text{ K}$). The metals are distributed over a wide range of densities and temperatures.

law, independent of the value of γ_{eff} imposed on their ISM gas (Schaye & Dalla Vecchia 2008).

- *Galactic winds* Galactic winds are implemented as described in Dalla Vecchia & Schaye (2008). Briefly, after a short delay of $t_{\text{SN}} = 3 \times 10^7 \text{ yr}$, corresponding to the maximum lifetime of stars that end their lives as core-collapse SNe, newly-formed star particles inject kinetic energy into their surroundings by kicking a fraction of their neighbouring gas particles in a random direction, as governed by,

$$\begin{aligned} \dot{M}_w &= \eta \dot{M}_* \\ \epsilon_{\text{SN}} f_w &= \frac{1}{2} \eta v_w^2. \end{aligned} \quad (3)$$

The mass loading factor, η , relates the rate at which mass is launched in a wind, \dot{M}_w , to the star formation rate, \dot{M}_* . The product ηv_w^2 , where η is the mass loading factor and v_w is the initial wind velocity, is proportional to the fraction f_w of the SN energy produced per unit mass, ϵ_{SN} , that powers the wind. We usually characterise the wind implementation by the mass loading factor, and wind speed.

The wind prescription is implemented as follows: each SPH neighbour i of a newly-formed star particle j has a probability of $\eta m_j / \sum_{i=1}^{N_{\text{ngb}}} m_i$ of receiving a kick with a velocity v_w . Here, the sum is over the $N_{\text{ngb}} = 48$ SPH neighbours of particle j . The REFERENCE simulation described below has a mass loading of $\eta = 2$ and wind speed of $v_w = 600 \text{ km s}^{-1}$ (i.e., if all baryonic particles had equal mass, each newly formed star particle would kick, on average, two of its neighbours, increasing their velocity by $v_w = 600 \text{ km s}^{-1}$). Assuming that each star with initial mass in the range $6 - 100 \text{ M}_\odot$ injects 10^{51} ergs of kinetic energy as it undergoes a core collapse SN, these parameters imply that the total

wind energy accounts for 40 per cent of the available kinetic energy for a Chabrier IMF and a stellar mass range $0.1 - 100 M_{\odot}$ (if we consider only stars in the mass range $8 - 100 M_{\odot}$ for type II SNe, this works out to be 60 per cent). The value $\eta = 2$ was chosen to roughly reproduce the peak in the cosmic star formation rate (Schaye et al. 2010). Note that contrary to the widely-used kinetic feedback recipe of Springel & Hernquist (2003), the kinetic energy is injected *locally* and the wind particles are *not* decoupled hydrodynamically. As discussed by Dalla Vecchia & Schaye (2008), these differences have important consequences.

• *Chemodynamics* We employ the method outlined in Wiersma et al. (2009). Briefly, a star particle forms with the elemental abundance of its parent gas particle. It then represents a single stellar population (SSP) with given abundance, and an assumed stellar IMF. The reference model uses the IMF proposed by Chabrier (2003), with mass limits of $0.1 M_{\odot}$ and $100 M_{\odot}$. At each time step, we compute the timed release of elements and energy from three stellar evolution channels: (i) core collapse SNe, (ii) type I SNe and (iii) asymptotic giant branch (AGB) stars. The stellar evolution prescriptions are based on the Padova models, using stellar lifetimes computed in Portinari et al. (1998) and the yields of low-mass and high-mass stars of Marigo (2001) and Portinari et al. (1998) respectively. The yields of Portinari et al. (1998) include ejecta from core collapse SNe (SNII) along with their calculations of mass loss from high-mass stars. Using these yields gives an element of consistency between the high- and low-mass stellar evolution. An e-folding delay time is used to describe the SNIa rate. The observed cosmic SNIa rate is approximately reproduced in the REFERENCE model with a fraction of 2.5% of white dwarfs that become SNIa, see Wiersma et al. (2009). We use the ‘W7’ SNIa yields of Thielemann et al. (2003).

Elements produced by nucleo-synthesis are distributed to SPH particles neighbouring the star, weighted by the SPH kernel, as done by e.g., Mosconi et al. (2001). The simulations track the abundance of the eleven individual elements that are important for the cooling and we use an extra ‘metallicity’ variable to track the total metal mass of each particle (see Wiersma et al. 2009). The ratio $Z \equiv M_Z/M$ of metal mass over total mass is the ‘particle metallicity’. For gas particles we also compute a ‘smoothed metallicity’ as $Z_{\text{sm}} \equiv \rho_Z/\rho$, i.e. the ratio of the metal density, ρ_Z , over the gas density, ρ , where both densities are computed using SPH interpolation. Stars inherit metal abundances of their parent gas particle: we record both the particle and smoothed metallicity. In Wiersma et al. (2009) we argued that the smoothed metallicity is more consistent with the SPH formalism than the particle metallicity. Using smoothed metallicities results in a spreading of metals over slightly greater volumes.

2.2 The Simulation Suite

Table 1 contains an overview the models from the OWLS suite that we consider here. Simulation names contain a string ‘LXXXNYYY’ which specifies the co-moving size of the periodic box, $L = \text{XXX} h^{-1}$ Mpc, and the number of particles $N = \text{YYY}^3$ of (initial) gas and dark matter; most runs discussed here have $L=25$ or 100 , and $N=512^3$. Comparing different L and N models allows us to investigate the effects of numerical resolution, and missing large-scale power. The table also contains a brief description of the physics in which a particular run differs from the REFERENCE model, see Schaye et al. (2010) and the next section for more details.

3 RESULTS

3.1 The reference model

We begin by describing the metal distribution of the REFERENCE_L100N512 simulation in temperature-density space at redshift $z = 0$ shown in Fig. 1.

It is useful to divide the $T - \rho$ plane into several ‘phases’, since, as we will show, different enrichment processes dominate in different phases, and also because the observational constraints for different phases are inferred from different types of data. A first division distinguishes between star-forming gas (henceforth SF gas) on the imposed $P - \rho$ relation (Eq. 1), which we identify with the ISM in galaxies, and non-star-forming gas (NSF gas). The SF gas can be seen as the thin band of contours on the right of figure 1 at $\rho/\langle\rho\rangle > 10^6$. We further divide NSF gas into *hot gas*, typically found in halos of large groups or clusters (ICM, $T > 10^7$ K), *warm-hot intergalactic and circum-galactic gas* (WHIM, $10^5 \text{ K} < T < 10^7 \text{ K}$), *diffuse gas* (diffuse IGM, $\rho < 10^2 \langle\rho\rangle$, $T < 10^5 \text{ K}$), and *cold halo gas* ($\rho > 10^2 \langle\rho\rangle$, $T < 10^5 \text{ K}$). These phases are indicated in Fig. 1. The colour coding indicates the mass-weighted mean metallicity for a given temperature and density. The metallicity shows a clear gradient with density, with the exception of the track of photo-ionised gas in the lower left hand corner, which has a very low metallicity. The contours, on the other hand, show the distribution of total metal mass. Metals are found at virtually all temperatures and densities, from the high-densities in galactic disks, to extremely low densities.

The spatial distribution of metals is shown at $z = 4, 2$ and 0 , in Fig. 2. At $z = 4$ (top left) metals are strongly clustered around haloes, with circum-halo metallicities of $\log(Z/Z_{\odot}) \approx -3$ to -2 , and large fractions of volume are enriched to exceedingly low levels, or not at all. As time progresses, circum-halo metallicities increase to $\log(Z/Z_{\odot}) \approx -2$ to -1 and the filling factor of metals also increases substantially, yet even at $z = 0$ (bottom right) there are still co-moving volumes which are barely enriched. Comparing the two resolutions (and box sizes), we note that although the abundance of circum-halo gas is similar at $z = 2$ in the L100N512 (bottom left) and L025N512 (top right) runs, the filling factor of metals is higher in the higher resolution simulation. Indeed, we showed in Wiersma et al. (2010) that lower density gas (which accounts for larger filling factors) was typically enriched by lower-mass galaxies, and higher resolution simulations probe the galaxy mass function down to lower masses.

We continue our analysis by comparing the metallicities and metal mass fractions in different phases provided by the reference simulation with observations. We then turn our attention to a comparison of the different OWLS models.

Fig. 3 shows the evolution of the metallicity³, metal mass fraction, and Ω_Z for various phases in the REFERENCE_L100N512 simulation. The fraction of metals in a given phase is simply the ratio of the metal mass in that phase over the total metal mass in the simulation. The amount of metals in a phase is shown as $\Omega_Z \equiv \langle\rho_Z\rangle/\rho_{\text{crit}}$, the ratio of the mean metal mass density in a given phase over the critical density. As the metal mass fraction and Ω_Z are much harder to measure observationally, and are in any case inferred from metallicity measurements, we only compare the

³ Note that for the remainder of this paper, we use ‘particle metallicities’ (see section 2.1), although since we are considering mean metallicities of a given phase, the results would have been virtually identical if we had used smoothed metallicities.

Table 1. Simulation Set

Name	Box Size (Mpc/h)		Description
AGN	25	100	Incorporates AGN model of Booth & Schaye (2009).
DBLIMFCONTSFV1618	25	100	Top-heavy IMF for $n_H > 30 \text{ cm}^{-3}$; $v_w = 1618 \text{ km s}^{-1}$
DBLIMFV1618	25	100	Top-heavy IMF for $n_H > 30 \text{ cm}^{-3}$; $v_w = 1618 \text{ km s}^{-1}$, $\dot{\Sigma}_*(0) = 2.083 \times 10^{-5} \text{ M}_\odot \text{ yr}^{-1} \text{ kpc}^{-2}$
DBLIMFCONTSFML14	25	100	Top-heavy IMF for $n_H > 30 \text{ cm}^{-3}$; $\eta = 14.545$
DBLIMFML14	25	100	Top-heavy IMF for $n_H > 30 \text{ cm}^{-3}$; $\eta = 14.545$, $\dot{\Sigma}_*(0) = 2.083 \times 10^{-5} \text{ M}_\odot \text{ yr}^{-1} \text{ kpc}^{-2}$
EOS1p0	25	100	Isothermal equation of state
EOS1p67	25		Equation of state $p \propto \rho^{\gamma_*}$, $\gamma_* = 5/3$
IMFSALP	25	100	Salpeter IMF, SF law rescaled
MILL	25	100	WMAP1 cosmology: $(\Omega_m, \Omega_\Lambda, \Omega_b h^2, h, \sigma_8, n, X_{\text{He}}) = (0.25, 0.75, 0.024, 0.73, 0.9, 1.0, 0.249)$
NOAGB_NOSNIa		100	AGB & SNIa mass & energy transfer off
NOHeHEAT	25		No He reheating
NOSN	25	100	No SNII winds, no SNIa energy transfer
NOSN_NOZCOOL	25	100	No SNII winds, no SNIa energy transfer, cooling uses primordial abundances
NOREION	25		No reionization
NOZCOOL	25	100	Cooling uses primordial abundances
REFERENCE	25	100	
REIONZ06	25		Redshift reionization = 6
REIONZ12	25		Redshift reionization = 12
SFAMPLx3	25		$\dot{\Sigma}_*(0) = 4.545 \times 10^{-4} \text{ M}_\odot \text{ yr}^{-1} \text{ kpc}^{-2}$
SFSLOPE1p75	25		$\gamma_{\text{KS}} = 1.75$
SFTHRESZ	25		Metallicity-dependent SF threshold
SNIaGAUSS		100	Gaussian SNIa delay distribution
WDENS	25	100	Wind mass loading and velocity determined by the local density
WHYDRODEC	25		Wind particles temporarily hydrodynamically decoupled
WML1V848	25	100	$\eta = 1$, $v_w = 848 \text{ km s}^{-1}$
WML4	25	100	$\eta = 4$, $v_w = 600 \text{ km s}^{-1}$
WML4V424	25		$\eta = 4$, $v_w = 424 \text{ km s}^{-1}$
WML8V300	25		$\eta = 8$, $v_w = 300 \text{ km s}^{-1}$
WThermal	25		SNII energy injected thermally
WVCIRC	25	100	‘Momentum driven’ wind model (scaled with the resident halo mass)

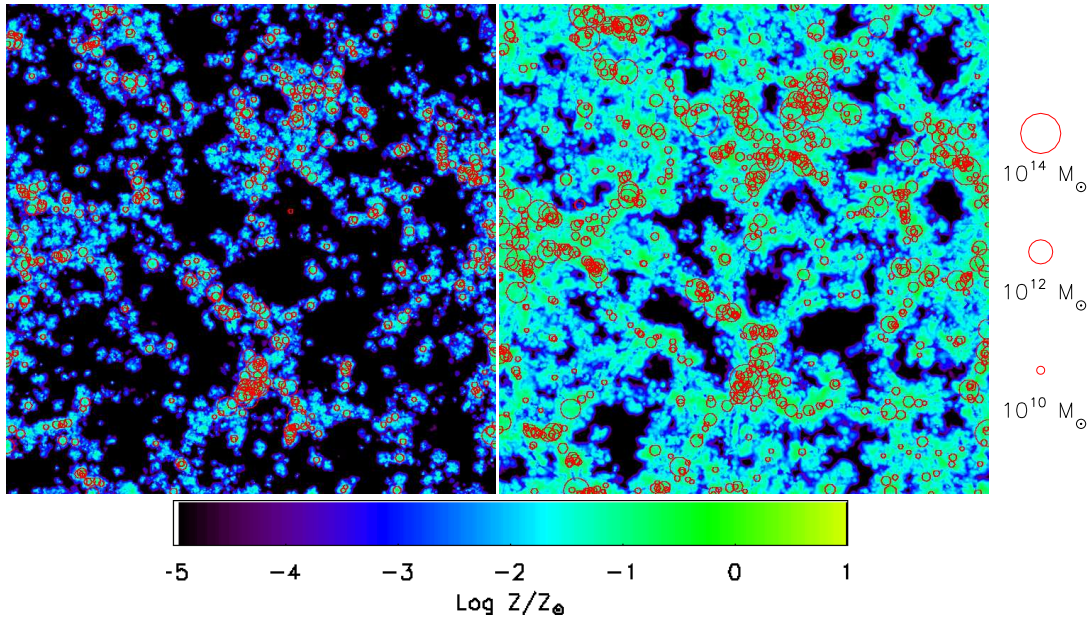


Figure 2. Metal distribution in the reference simulations. Shown are $5h^{-1}$ Mpc (comoving) thick slices through the REFERENCE_1025N512 simulation (top row) at $z = 4$ (left), and $z = 2$ (right) and through the REFERENCE_100N512 simulation (bottom row) at $z = 2$ (left), and $z = 0$ (right). The colour coding shows (SPH-smoothed) metallicity, mass averaged along the line of sight; the colour scale is cut off below $\log(Z/Z_\odot) = -5$ although metallicities extend to lower values. Red circles correspond to haloes identified by a friends-of-friends group finder, with radius proportional to the logarithm of the stellar mass of the halo, as indicated to the right of the panels. Metals are initially strongly clustered around haloes, but their volume filling factor increases as time progresses.

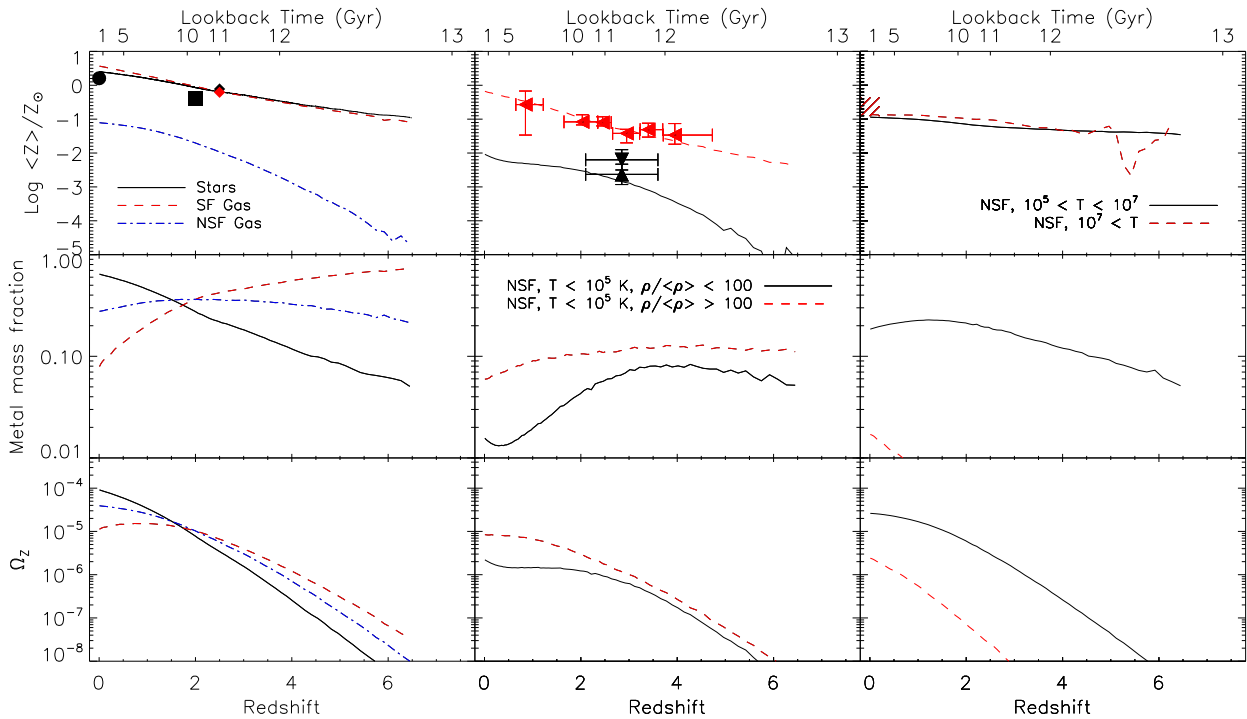


Figure 3. Metallicity (top row), metal mass fraction (middle row), and Ω_Z (bottom row) as a function of redshift for the various phases of baryons in the REFERENCE_L100N512 simulation. Curves indicate simulation results, with different line styles indicating various baryonic phases. *Left column:* stars (solid black), SF gas (dashed red), NSF gas (dot-dashed blue); *Middle column:* diffuse IGM (black), cold halo gas (dashed red); *Right column:* WHIM (solid black line), ICM (dashed red). Data points indicate observations and are colour-coded to indicate to which phase they should be compared. The diamonds at $z = 2.5$ are estimates of stellar and star-forming metallicities by Pagel (2008), with further stellar metallicities indicated by a circle (Gallazzi et al. 2008) and a square (Halliday et al. 2008). DLA measurements are from Prochaska et al. (2003, solid, left pointing triangles), IGM pixel optical depth measurements in QSO spectra are from Aguirre et al. (2008, open triangle pointed down) and Schaye et al. (2003, open triangle pointed up). The ICM measurements are from X-ray observations (Simionescu et al. 2009, hatched region).

predicted metallicities with observations and will mostly focus on metallicities in the rest of this work.

Now we briefly walk through the data (which we have converted to our adopted solar abundances) to which we are comparing:

- *Stars* For stellar metallicities, we compare to the global values obtained by Gallazzi et al. (2008, circle in the top-left panel) for $z = 0$ and Halliday et al. (2008, square in top left panel) for $z = 2$. Halliday et al. (2008) note that their metallicities are lower than those of Erb et al. (2006) and speculate that since Erb et al. (2006) observed oxygen, a non-solar $[O/Fe]$ ratio might make their observations agree. We have also compared their point to $[Fe/H]$ and indeed find a better match to the data. The $z = 2.5$ point is taken from Bouché et al. (2007) which is compiled from their own previous measurements.

- *Star-forming gas* Bouché et al. (2007) give a value for ISM and/or dust at $z = 2.5$ and, following Pagel (2008), we include it here as a filled red diamond in the top-left panel.

- *Diffuse IGM* We have included the carbon and oxygen Lyman- α forest measurements from Schaye et al. (2003, upwards pointed triangle in the top middle panel) and Aguirre et al. (2008, downwards pointed triangle in the top middle panel), respectively.

- *Cold Halo Gas* While the precise nature of DLAs is still somewhat uncertain, we surmise that circum-halo and intrahalo cold gas most likely have higher cross-sections than the ISM and we thus

assume that observations of DLA and sub-DLA systems trace cold halo gas. As such, we have plotted the compilation of DLA metallicities from Prochaska et al. (2003, leftwards pointed triangles in the top middle panel).

- *WHIM* The WHIM has long stood as a phase that is thought to contain a large fraction of the baryons and metals, but is difficult to detect. As such, there is no direct measurement of the metallicity of the WHIM.

- *ICM* Measurements of ICM metallicities are also troublesome, although much less so than for the WHIM. The main difficulty is measuring the metallicity out to large enough radii in order to get a good estimate of the mean metallicity. We have chosen to use the outermost measurements of cluster metallicities by Simionescu et al. (2009, hatched region in the top right panel), using a box to indicate the range of values in their sample.

The metallicities of our simulation follow the trends seen in the data. We reproduce the observed increase with cosmic time of the stellar and cold halo metallicities (although our stellar metallicities fall slightly above the observed points). The high-redshift measurements for the star-forming gas are satisfied as well. The predicted metallicity of the $z \approx 3$ diffuse IGM agrees with the measurement for carbon (Schaye et al. 2003), but is about 0.5 dex lower than the observed value for oxygen (Aguirre et al. 2008), which should be closer to the overall metallicity. Our prediction for the intracluster metallicity is within the observed range.

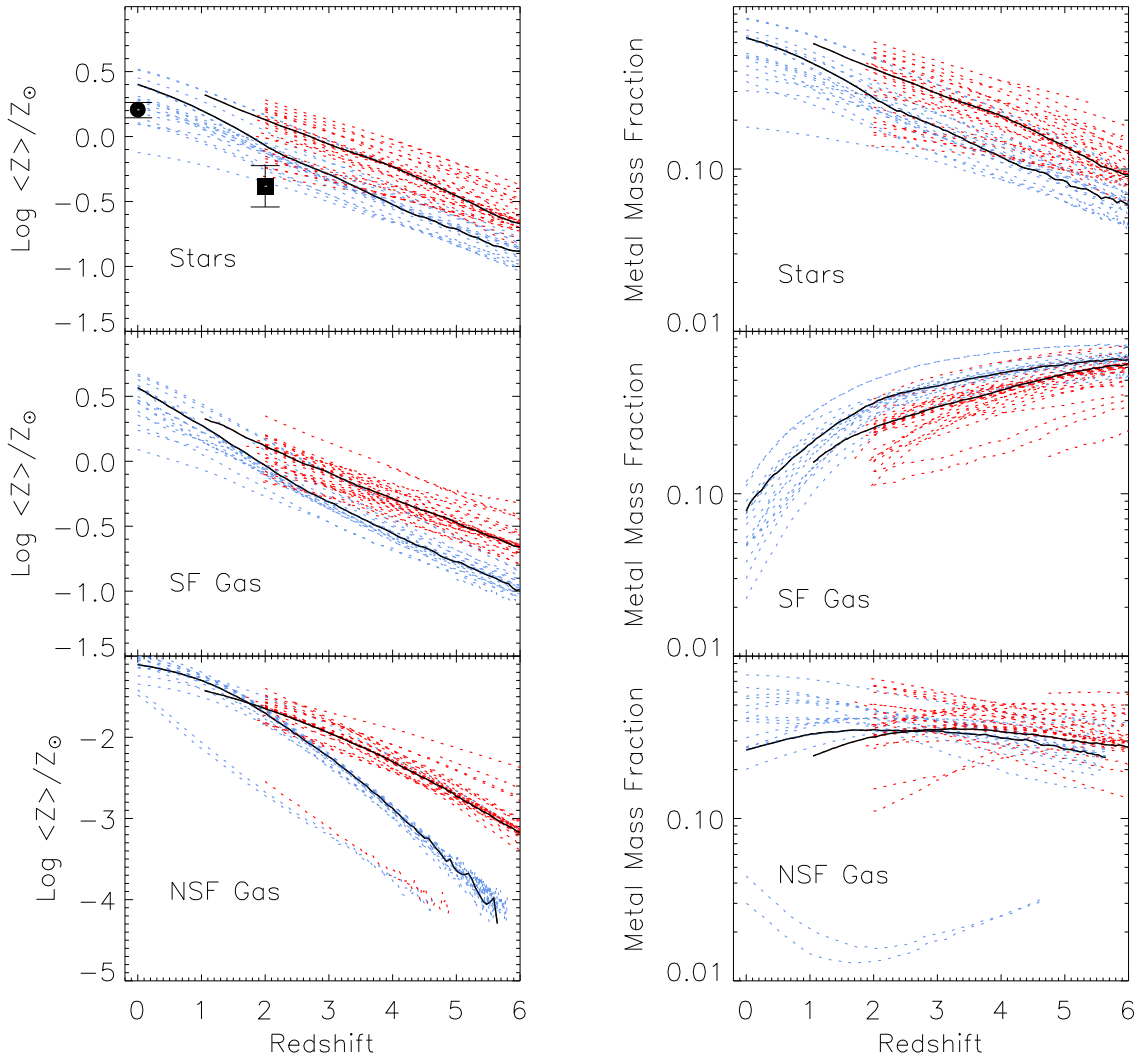


Figure 4. Mean metallicity (left) and metal mass fraction (right) for stars (top), star-forming gas (middle), and non-star-forming gas (bottom) as a function of redshift for all OWLS simulations. Shown are the REFERENCE simulations (solid black), the rest of the L025N512 simulations (dotted red,) and the rest of the L100N512 simulations (dotted blue). The higher resolution (L025N512) simulations were stopped at $z = 2$ (with the exception of the REFERENCE model which was stopped just above $z = 1$), but the lower resolution simulations (L100N512) were continued to $z = 0$. The mean stellar metallicity in units of solar rises from ~ -0.5 dex at $z = 6$ to supersolar at $z = 0$, closely tracking the metallicity of the SF gas. For these two phases, resolution plays a minor role, with a 64 times higher mass resolution resulting in about 0.2 dex higher metallicities. The metallicity of NSF gas is, however, strongly resolution dependent for $z > 2$. In the higher resolution simulation it rises from $\text{Log}(Z)/Z_{\odot} \approx -3$ at $z = 6$ to -1 at $z = 0$. Points with error bars indicate observations of stellar metallicities at $z = 0$ and $z = 2$ by Gallazzi et al. (2008) and Halliday et al. (2008), respectively. The stellar metal mass fraction increases towards $z = 0$, whereas the metal mass fraction in SF-gas decreases slowly to $z \approx 2$, then falls much more rapidly. Aside from the models without feedback (the group of very low curves in the bottom panels; note that NOSN_L025N512 and NOSN_NOZCOOL_L025N512 fall on top of each other in the left panel and fall below the plotting area in the right panel), most of the different runs yield results that follow the REFERENCE model relatively closely, indicating that the predicted metallicities are reasonably robust to model variations.

3.2 Overview

We want to investigate which physical processes determine the cosmic metal distribution in a given phase. We begin by discussing some of the overall trends that are present in nearly all of our models. Fig. 4 shows the evolution of the metallicity (left) and the metal mass fraction (right) for stars (top), SF gas (middle), and NSF gas (bottom). The black curves show the results for the reference model, with the curve that continues down to $z = 0$ indicating the 100 Mpc/h box. Blue and red curves indicate the results for the 100 and 25 Mpc/h boxes for all other models.

The metallicities of the SF gas and stars track each other very

closely, increasing steadily from $\log(Z/Z_{\odot}) \sim -0.5$ at $z = 6$ to supersolar values at $z = 0$. While the metal mass fraction contained in stars increases with time, from $\sim 10^{-1}$ at $z = 6$ to $0.2-0.9$ at $z = 0$, the fraction of the metal mass contained in SF gas decreases with time, and does so more rapidly for $z < 2$. All models predict that by $z = 0$ SF gas accounts for only a small fraction of the metal mass. The rapid decrease in the metal mass fraction in SF gas for $z < 2$ reflects the decrease in the cosmic star formation rate (Schaye et al. 2010) and hence the global mass density of SF gas. While the metallicity of the NSF increases rapidly with time, from $\sim 10^{-3} Z_{\odot}$ at $z = 6$ to $10^{-1} Z_{\odot}$ at $z = 0$, the fraction of the

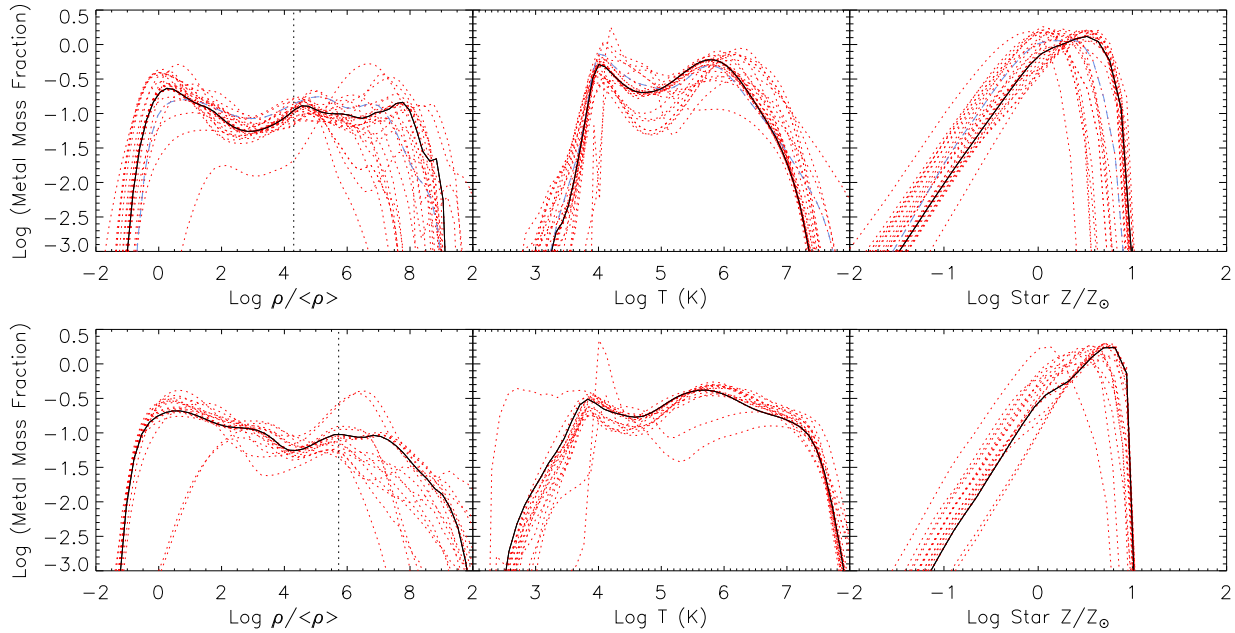


Figure 5. The left and middle panels show the fraction of metals in gas as a function of density and temperature, respectively, and the right panels shows the fraction of metals in stars as a function of stellar metallicity. The top and bottom rows show $z = 2$ and 0 , respectively. Each histogram is normalised such that it sums to unity. The reference simulations are shown as solid black, while the rest of the simulations are shown in dotted red. The REFERENCE_L100N512 model at $z = 2$ is shown in the top panel with the dashed blue line. SF gas is omitted from the central panel, since the ‘temperature’ of this multi-phase gas is set by the imposed $P - \rho$ relation. The dotted vertical lines indicate the star formation threshold. While there are a few outliers, most models yield similar metal distributions, with the largest differences occurring at high ρ and small T .

metals residing in this diffuse phase is relatively constant and, except for models without any feedback, always significant (for both reference simulations this fraction stays between 20% and 35% between $z = 6$ and $z = 1$). Initially, the majority of the metals reside in SF gas. At $z \approx 3$ metals are approximately equally distributed over the three different phases (stars, SF and NSF gas), with stars becoming the dominant repository of metals at lower redshift.

Comparing the two different box sizes (blue vs red curves), for which the mass resolution differs by nearly two orders of magnitude, we see that the results for stars and SF gas are surprisingly (given the enormous change in resolution) well converged. The higher resolution runs predict stellar metallicities and metal mass fractions that are about 0.2 dex higher. For SF gas the metallicity is also slightly higher (about a factor of two at $z = 6$ and less at lower redshifts), but the metal mass fraction is slightly lower, because there is more gas in this phase in higher resolution runs. The metallicity of NSF gas is much more sensitive to the resolution and is unreliable in the lower resolution simulations above $z \approx 2$. The fact that the two different resolutions yield similar metal mass fractions for NSF gas at high redshift is a coincidence, caused by the fact that there are far fewer metals in the lower resolution runs.

We recall the results of the more extensive numerical convergence tests performed for the reference model in appendices B and C of Wiersma et al. (2009). For metallicity and metal mass fraction, except possibly for the ICM, our simulation boxes are sufficiently large. On the other hand, resolution proves to be much more of a challenge. The stellar metal mass fraction just barely converges for the L025N512 resolution, although the difference is small by $z = 2$. The metal mass fraction in the cold-phase NSF gas is converged to within a factor of two. Obtaining converged results tends to be more challenging at higher redshifts. Metallicity is generally better converged than the fraction of metals in a given phase,

and is reasonably reliable for all phases at the resolution of the L100N512 simulations, with the exception of the metallicity of the diffuse IGM. Higher resolution simulations generally yield higher metallicities, especially at higher redshift, but even in this phase, the simulations are converged by $z = 2$ ($z = 3$) for L100N512 (L025N512) runs.

The distributions of metals at $z = 0$ and $z = 2$ are investigated in more detail in Fig. 5. The metal mass weighted probability distribution function (PDF)⁴ shows several maxima in both density and temperature, with minima at $\rho \sim 10^3 \langle \rho \rangle$ and $\rho \sim 10^4$ at $z = 2$ and $z = 0$ respectively, which corresponds to $n_H \sim 10^{-3} \text{ cm}^{-3}$ in both cases, and at $T \approx 10^5 \text{ K}$.

All models have a relatively well pronounced maximum at $\rho \sim \langle \rho \rangle$, which is due to the fact that there are very few metals in underdense gas and that gas that is much denser quickly accretes onto haloes. The outliers at the low-density end of the distribution result from turning off feedback (see Fig. 6), while the outliers at the high-density end correspond to either strong feedback models (e.g. AGN) or models in which the star formation efficiency is increased (e.g. SFAMPLX3).

The temperature minimum in the metal mass fraction at $T \sim 10^5 \text{ K}$ is caused by a number of factors. First, gas cooling is very efficient at this temperature. Second, the winds tend to shock metals to temperatures higher than this value, causing a peak in the distribution at higher temperatures. Finally, the equilibrium temperature due to photo-heating is lower than this temperature, caus-

⁴ We emphasise that the right most panel does *not* show the metallicity distribution function, as is commonly plotted. It rather shows how the metal mass is distributed among stars of various metallicities, which is more heavily weighted towards higher metallicities than the metallicity distribution function.

ing a second peak at $T \sim 10^4$ K. The temperature distribution of the metals shows less variation than the distribution with density. The two outliers again correspond to models without feedback (see Fig. 6). Such models have little shock-heated metals, resulting in much more low temperature metals. Without metal cooling, these metals pile up at 10^4 K, whereas with metal cooling the metals are found to very low temperatures. This effect is diminished at $z = 2$, although note that the NOSN_L025N512 simulation is not shown because it was stopped at $z \approx 3$ due to computational costs.

The distribution of metals over stars with different metallicities (right panels) is similar in the different models, with the main deviation at high metallicity being due to the AGN simulation, which predicts more metal mass in lower metallicity stars.

These figures once more illustrate the large dynamic range in density and temperature over which metals are distributed. These distributions are mostly converged with respect to both box size and resolution (Figs. B3 and C3 of Wiersma et al. 2009), with some dependence of the temperature distribution on box size, and of the density distribution on resolution. Next, we will investigate in more detail how various physical processes affect the metal distribution.

3.3 Impact of galactic winds and metal-line cooling

In this section we discuss the effect of including galactic winds driven by SNe and metal-line cooling on the metal distribution. We show that outflows are essential for enriching the IGM and that metal-line cooling strongly affects the temperature distribution of metals. On the other hand, the hot non-star-forming gas can obtain rather high metallicities without feedback, indicating that the ICM is enriched at least partly by some process that is not directly related to SN feedback.

Fig. 6 compares the REFERENCE simulation to a simulation without metal cooling (NOZCOOL), one without winds (NOSN; note that the blue lines in the lower left panel fall mainly under the green lines), and one with neither metal cooling nor winds (NOSN_NOZCOOL). These simulations differ not only in the way metals are distributed, but also in their star formation histories since cooling and feedback of course also affect the conversion of gas into stars (see Schaye et al. 2010).

The top panels shows metal mass weighted PDFs at $z = 0$. The simulation without metal cooling contains fractionally more metals than the REFERENCE model at $\rho \sim 10^2 \langle \rho \rangle - 10^4 \langle \rho \rangle$ at the expense of metals in the ISM. Metal cooling thus allows metals to condense from haloes into star-forming gas. This clearly illustrates the importance of metal cooling for gas accretion onto star-forming regions. Surprisingly, the presence of metal cooling has little effect on the temperature distribution where the cooling curve peaks ($T \approx 10^5$ K). This is most likely because the cooling times here are already short. Metal cooling does reduce the fraction of metals at $T \sim 10^{6.5}$ K. The largest difference is noticed in the low temperature regions (we remind the reader that the temperature distribution excludes gas with densities above our star-formation threshold). Metals can cool gas well below 10^4 K, while neglecting metal cooling abruptly cuts the distribution off, although there are still some metals with $T < 10^4$ K due to adiabatic cooling. Finally, metal cooling slightly increases the fraction of metals locked up in high metallicity stars.

In the absence of galactic winds, only a negligible fraction of the metals reach densities $\rho \lesssim 10 \langle \rho \rangle$ (top-left panel of Fig. 6). This underlines the importance of feedback in reproducing the metals seen in the IGM. Note that this is in opposition to Gnedin (1998) who found that feedback played only a minor role in enrich-

ing the IGM, but agrees well with Aguirre et al. (2001,?). Winds also serve to evacuate metals from the ISM as we can see that in the absence of feedback, metals tend to pile up just above the star-formation threshold. Without winds, the fraction of metals at (NOSN_NOZCOOL) or below (NOSN) 10^4 K is much higher than in any model that includes feedback from SNe (top-middle panel of Fig. 6), because the metals reside in gas with higher densities and metallicities and thus higher cooling rates. Winds strongly boost the fraction of metals in gas with $10^5 \text{ K} < T < 10^7 \text{ K}$, which suggests that wind shocks may also shape the metal distribution at these temperatures. As expected, galactic winds shift the metals locked up in stars to lower stellar metallicities.

In the bottom panels of Fig. 6 we show the metallicities of various phases as a function of redshift. As discussed in Wiersma et al. (2009), in the REFERENCE model most of the metals are initially in the gas phase, while by the present day the majority of the metals are locked up in stars. The effect of neglecting metal cooling is small for the metallicity of either stars or SF gas, but is obvious for the metallicity of the IGM (which is *lower* by up to an order of magnitude in the absence of metal cooling) and the WHIM (*higher* by ≈ 0.2 dex without metal cooling).

Without winds, more metals are in stars and significantly fewer in NSF gas, but the metallicities of stars, SF gas, dense NSF gas, and ICM are in fact not very different. The absence of feedback has a major effect on the metallicity of the IGM (low T and low ρ NSF gas) and the WHIM (hot, NSF gas), decreasing their metallicities by more than 2 and 1-2 orders of magnitude, respectively. Without galactic winds, metals are not efficiently transported to the lower densities of the diffuse IGM or WHIM. A careful census of the IGM metallicity, and its evolution, is therefore a powerful probe of the properties of galactic winds through the ages. On the other hand, the metallicity of the ICM is hardly affected by the presence of winds, suggesting that dynamical processes such as ram pressure stripping dominate the enrichment of this phase.

In summary, feedback from SNe is essential for enriching the gas outside of haloes and increase the fraction of the metals in warm-hot gas. Metal-line cooling, on the other hand, shifts the metal distribution towards lower temperatures and, provided winds are present, strongly increases the fraction of metals in the ISM. The metallicity of the present day ICM is $\sim 10^{-1}$ solar and is remarkably insensitive to the presence of feedback and metal cooling. This implies a minimum metallicity for the ICM, and an enrichment mechanism that is not related to galactic winds.

3.4 Different implementations for galactic winds

In the previous section we simply turned off galactic winds. Here we will investigate what happens if we vary the implementation of the outflows. We will show that the metallicity of the IGM is particularly sensitive to the implementation of feedback, some models are quite capable of enriching this low-density gas while others cannot. On the other hand, the metallicities of the stars and the star-forming gas are largely robust to differences in the wind model. The ICM and WHIM maintain a relatively constant metallicity with redshift if the feedback recipe is varied.

Winds in most of the simulations comprising the OWLS suite are characterised by two parameters: the mass loading factor, η , and the initial wind speed, v_w (Dalla Vecchia & Schaye 2008; Eq. 3). All models shown in Fig. 7 use the same value of the product ηv_w^2 and hence they assume that the same fraction of core collapse SN energy is used to power winds. The wind speed sets an approximate maximum depth of the potential well out of

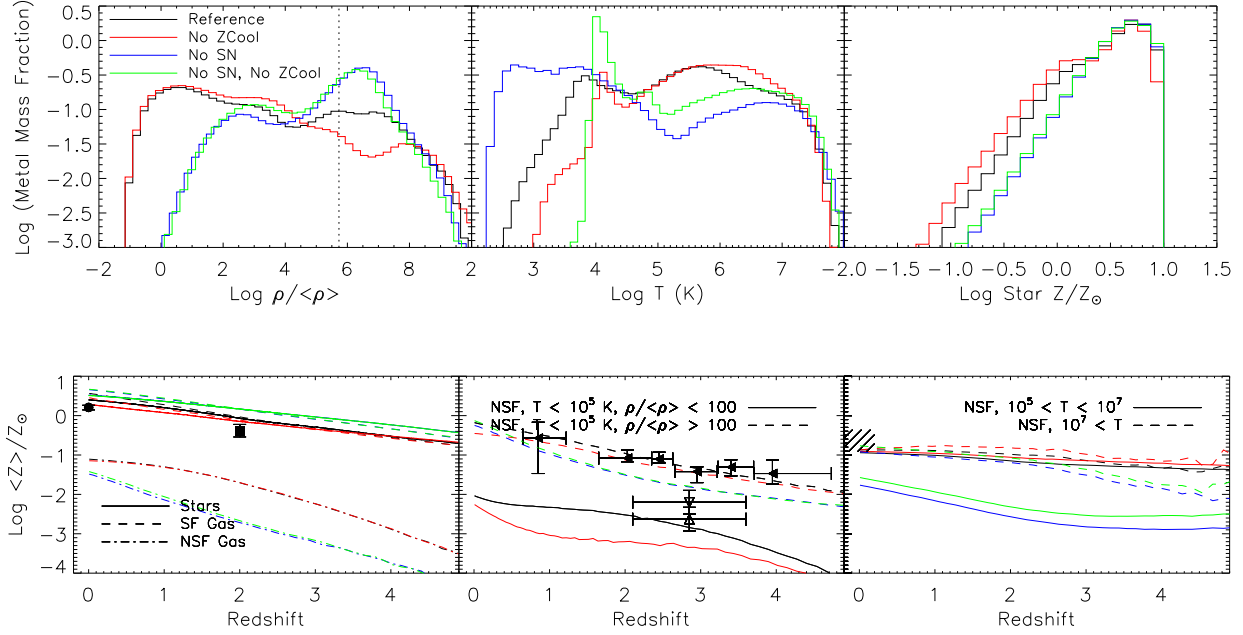


Figure 6. Distribution of metals for L100N512 simulations with different feedback and cooling prescriptions. *Top panels:* $z = 0$ metal mass weighted PDFs of gas density, temperature, and stellar metallicity. Each PDF is normalised to unity. In the left-most panel, the star formation threshold ($n_{\text{H}} = 10^{-1} \text{ cm}^{-3}$) is indicated by the dotted line. ISM gas was removed from the temperature PDF. *Bottom panels:* Metallicity as a function of redshift for the phases as defined in Fig. 1. The left panel shows stars (solid), SF gas (dashed) and NSF gas (dot-dashed). The middle panel shows cold IGM (NSF, $\rho < 10^2 \langle \rho \rangle$, $T < 10^5 \text{ K}$; solid), and cold halo and circum-halo gas (NSF, $\rho > 10^2 \langle \rho \rangle$, $T < 10^5 \text{ K}$; dashed). Finally, the right panel shows the WHIM (NSF gas, $10^5 \text{ K} < T < 10^7 \text{ K}$; solid) and the ICM (non-star-forming, $T > 10^7 \text{ K}$; dashed). Shown are the REFERENCE simulation (black), a simulation which ignored metal cooling (NOZCOOL; red), a simulation without galactic winds driven by SNe (NOSN; blue), and a model with neither winds nor metal cooling (NOSN_NOZCOOL; green), as indicated in the top left panel. Note that the metallicity of the diffuse IGM for the simulations without feedback is below the plotted range in the bottom-middle panel. Data points indicate observations as in Fig. 3, where the points in the left panel correspond to stellar metallicities, the solid triangles in the middle panel correspond to the cold halo gas while the open triangles show diffuse IGM measurements and the hatched region in the right panel shows an ICM metallicity measurement. Metal cooling shifts the metal distribution towards lower temperatures and increases the fraction of metals in the ISM. Galactic winds are crucial for the enrichment of low-density gas. The metallicity of the ICM is insensitive to both metal cooling and galactic winds.

which the wind can push baryons: star formation will no longer be quenched significantly in a galaxy for which wind particles cannot escape. Note that since winds are quenched due to drag forces in the ISM, which depend on its pressure and hence on the mass of the galaxy, the relationship between the wind speed required for escape and the potential well of the halo is non-trivial (see Dalla Vecchia & Schaye 2008). This parametrisation of winds is still very simple with little physical motivation. Given the coarse resolution of cosmological simulations, wind models should be guided by observations. Unfortunately, relating the wind parameters to observations is problematic, because the wind mass loading and velocity will vary with radius (which is poorly constrained for measurements based on absorption lines), inclination, and gas phase. For a complete description of the method and further motivation see Dalla Vecchia & Schaye (2008).

At high z , when most stars form in low-mass galaxies, even a low value of v_w may enable the gas to escape from most galaxies. For constant ηv_w^2 , a low wind speed implies high mass loading and hence a strong suppression of early star formation. Metals are then very efficiently transported out of the galaxies, and end up predominantly in the cold NSF gas, since the wind velocities are low enough that strong shocks do not occur. However, as time progresses, a low wind speed model can no longer suppress star formation in the increasingly more massive galaxies. The metals that are produced can no longer escape from the haloes and remain in the SF gas. For higher values of v_w metals can escape from typi-

cal star-forming galaxies up to far lower z and end up in hotter gas because the winds get shocked to higher temperatures.

The dependence of the $z = 2$ metal distribution on the wind speed and mass loading is shown in the top row of Fig. 7 for models that all use constant η and v_w , identical ηv_w^2 , but for which η varies by a factor of 8 (and thus v_w by a factor of $\sqrt{8}$). As expected, a higher v_w results in a larger fraction of metals residing in gas with low density and high temperature. Conversely, low- v_w models have a considerably larger fraction of their metals at high density, and low temperature ($T \sim 10^4 \text{ K}$). The low mass-loading model shows a peak in the density distribution of the metal mass just above the star formation threshold (vertical dotted line) that is similar to the reference model, indicating that the location of this peak is not set by the wind velocity (although the width and the height certainly are). There is another small peak at $\rho \sim 10^{7.5} \langle \rho \rangle$ in the metal-mass weighted density PDF of the low mass-loading model, which may be due to the largest haloes which have such high ISM pressures that even these high-velocity winds are quenched. The metal mass distributions in temperature show how higher wind velocities lead to more metals in hotter gas, due to metals in winds getting shocked to higher temperatures. A large portion of metals that are at $T \sim 10^5 \text{ K}$ in the REFERENCE model are heated to $\gtrsim 10^6 \text{ K}$ for $v_w = 848 \text{ km s}^{-1}$. The stellar metal mass PDF shifts to slightly lower metallicities for higher v_w .

While the distribution of the metals depends very strongly on the wind model, there is relatively little difference in the *metallicity*

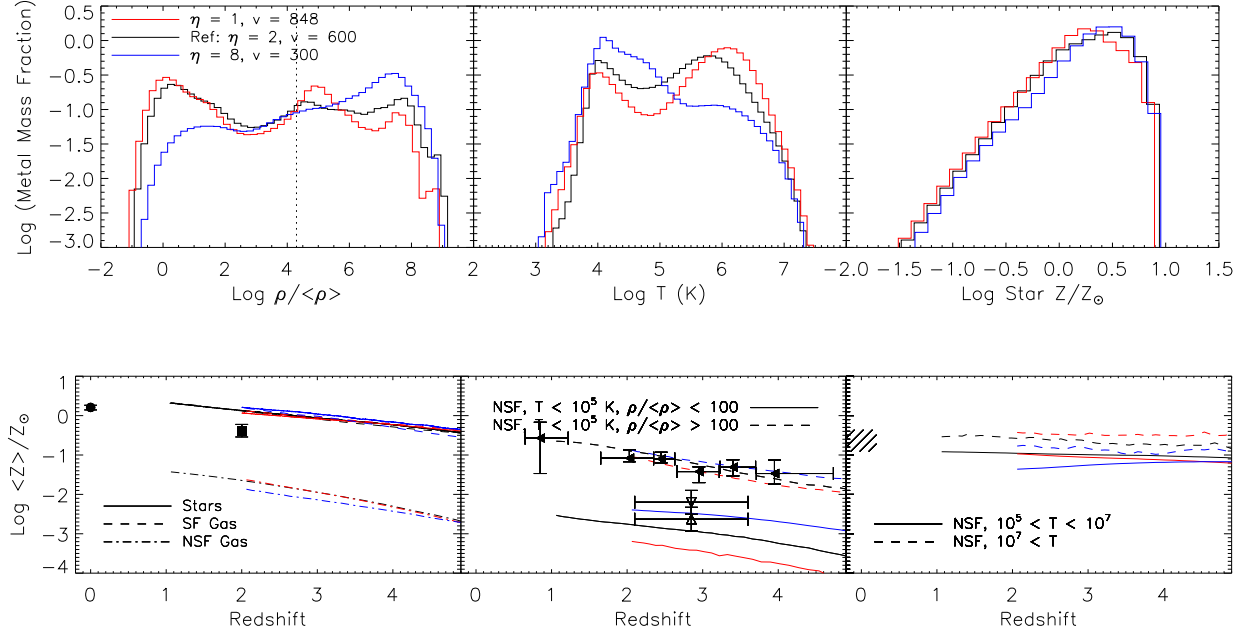


Figure 7. As Fig. 6, but for L025N512 simulations with different values for the mass loading, η , and wind speed, v , but identical values for ηv^2 and thus for the wind energy per unit stellar mass formed. The metal mass weighted PDFs (top row) are for $z = 2$. Compared are the REFERENCE simulation ($\eta = 2$, $v_w = 600$ km s $^{-1}$; black), a simulation using a mass-loading of 1 ($\eta = 1$, $v_w = 848$ km s $^{-1}$; red), and a simulation using a mass-loading of 8 ($\eta = 8$, $v_w = 300$ km s $^{-1}$; blue). The density and temperature distributions of metals are strongly dependent on η , with higher values of η shifting metals to higher gas densities and lower temperatures. Only the metallicity of the IGM is significantly affected, with higher η yielding higher metallicities.

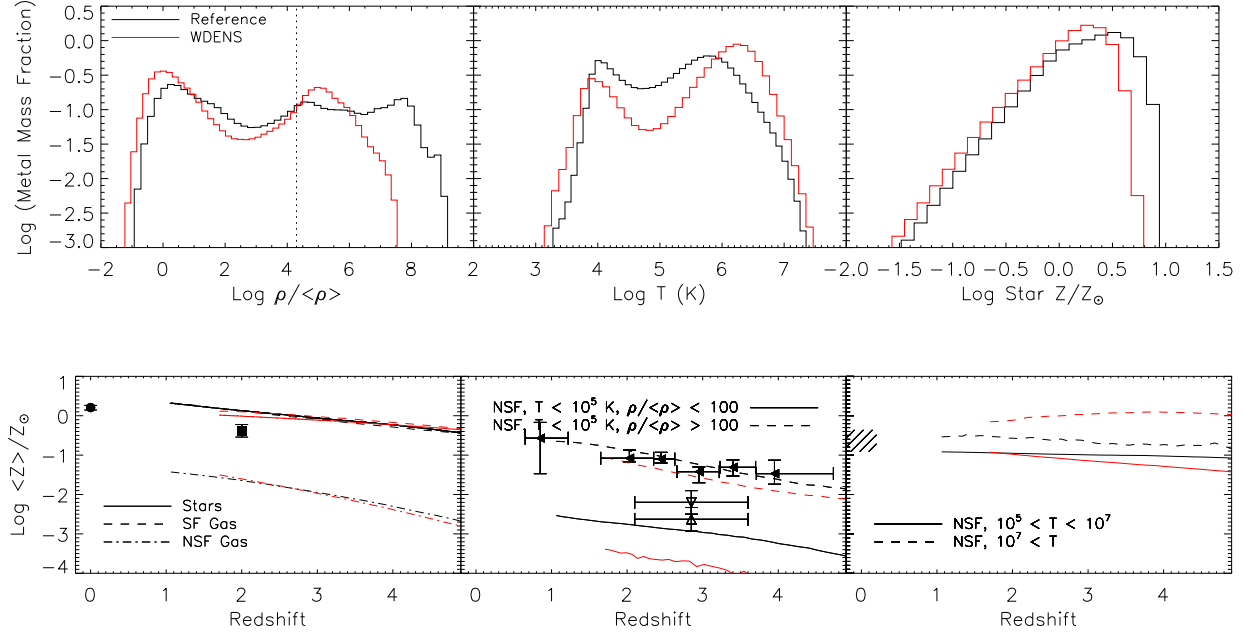


Figure 8. As Fig. 6, but for L025N512 simulations comparing the REFERENCE simulation (black) to model WDENS (red) in which wind speed is proportional to the local sound speed, while keeping the the wind energy per unit stellar mass formed identical to that in the REFERENCE model (Eq. 5). The metal mass weighted PDFs are for $z = 2$. The metallicities of both stars and SF gas are similar between these models, but the top-left panel shows that lowest density gas is significantly *more* enriched in the WDENS model. Nevertheless, the middle bottom panel shows that the metallicity of the cold IGM though is lower in the WDENS model, which is due to the fact that the metals are hotter in this model.

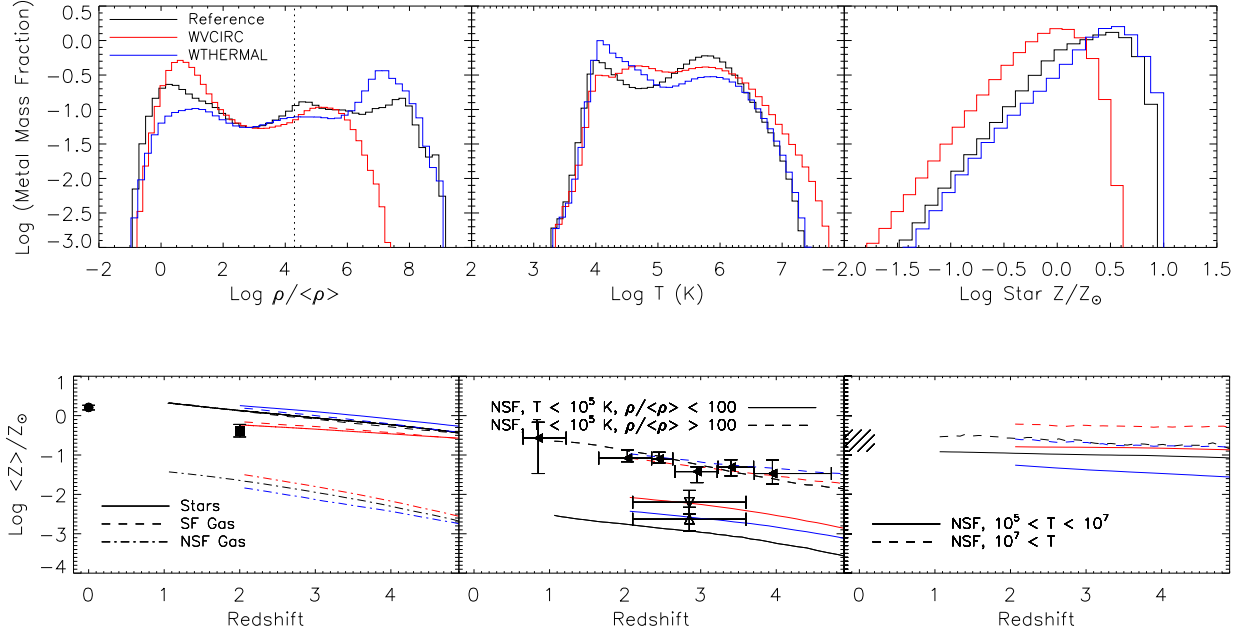


Figure 9. As Fig. 6, but for L025N512 simulations, comparing the REFERENCE simulation (black) to model WVCIRC (red), in which wind speed depends on the depth of the potential well (Eq. 6), and to model WThermal in which SN energy is injected thermally (blue). While WThermal uses the same wind energy per unit stellar mass as the REFERENCE model, the energy increases with halo mass for model WVCIRC (and can exceed that available from star formation). The metal mass weighted PDFs are for $z = 2$. Model WVCIRC is able to evacuate metals from high-density regions, while at the same time, spreading the metals over a variety of temperatures. Model WThermal differs less dramatically from the REFERENCE model, with more metals ending up in high-density regions.

between models with different v_w , with the exception of the metallicity of the IGM. In particular, the stellar and SF gas abundances are only marginally affected by the value of v_w for the range of parameter values that we investigated. The metallicities of both the WHIM and the ICM remain strikingly constant with time at ≈ -1 and ≈ -0.5 , respectively, all the way from $z = 6$ to $z = 1$ and, as shown in Fig. 6, even to $z = 0$. These values are clearly relatively robust with respect to the wind implementation.

The IGM metallicity in the high-mass-loading ($\eta = 8$) model is nearly an order of magnitude higher than in the low-mass-loading ($\eta = 1$) model, despite the fact that a much smaller fraction of the metal mass resides at densities $\rho < 10^2 \langle \rho \rangle$ for $\eta = 8$. The increase in the metallicity of the IGM (which has $T < 10^5$ K by definition) with decreasing v_w must therefore be due to a decrease in the temperature of the enriched low-density gas. The $\eta = 8$ model gives better agreement with the value inferred for the oxygen abundance by Aguirre et al. (2008), and is well within the uncertainties of the Schaye et al. (2003) value for carbon. Because most of the metals in the IGM are ejected by low-mass galaxies (see Booth et al. 2010; Wiersma et al. 2010) from which even low-velocity winds can remove gas, a large mass-loading enriches the low-density IGM much more efficiently.

In model WDENS the fraction of SN energy that powers the wind, $\epsilon_{\text{SN}} \propto \eta v_w^2$ (Eq. 3), is still kept fixed to the value used in the reference model, but v_w scales with the local sound speed, c_s . Since star-forming gas is on an imposed $P - \rho$ relation (Eq. 1), $c_s^2 \propto P/\rho \propto \rho^{\gamma_{\text{eff}}-1} \propto \rho^{1/3}$ for our assumed value of $\gamma_{\text{eff}} = 4/3$. The assumed wind parameters therefore depend on the density:

$$v_w = v_0 \left(\frac{n_H}{n_{H;\text{thres}}} \right)^{1/6} \quad \text{and} \quad (4)$$

$$\eta = \eta_0 \left(\frac{n_H}{n_{H;\text{thres}}} \right)^{-2/6} \quad (5)$$

where $n_{H;\text{thres}}$ is the star formation threshold density. We chose $v_0 = 600 \text{ km s}^{-1}$ and $\eta_0 = 2$, so that the wind parameters are the same as in the REFERENCE model at the star formation threshold. Compared with the REFERENCE model, the winds in WDENS will remain efficient in regulating star formation for denser gas at the bottom of deeper potential wells, where the winds will have higher v_w .

Figure 8 confirms that model WDENS is able to reduce the build up of metals in high-density gas and the fraction of metals locked up in high-metallicity stars. In general, WDENS continues the trend with increasing v_w shown in Fig. 7. The high-density tail is truncated at $\rho/\langle \rho \rangle \sim 10^7$. The higher wind speeds result in a larger fraction of metals at $T > 10^6$ K due to winds getting shocked. With fewer metals in high-density SF gas, stellar metallicities are on average ≈ 0.1 dex lower than in the REFERENCE model. The ICM is enriched to higher levels at nearly solar, with little evolution. We note, however, that at these high redshifts the ‘ICM’ consists largely of hot, low-density gas shocked by galactic winds. As we will show below (see Fig. 13), for $z = 0$ model WDENS predicts ICM metallicities that are only slightly greater than for the reference model. The enrichment of the cold IGM is notably less advanced than in the REFERENCE model, with a metallicity nearly 1 dex lower, in spite of the larger fraction of metals at low densities. This is again because the faster winds shock-heat more of the escaping metals to temperatures for which the cooling time is long.

In model WDENS the wind speed scales with the local sound speed to obtain efficient feedback in low-mass galaxies at early

times⁵ as well as in more massive haloes at later times. An alternative method to obtain a similar behaviour makes the wind speed depend directly on the depth of the potential well, as in the model discussed by Oppenheimer & Davé (2008), which is meant to mimic a case where the wind is driven by radiation pressure. Such a wind is implemented in our WVCIRC model as follows: an on-the-fly friends-of-friends group finding algorithm is used to identify haloes and their circular velocities, $v_{\text{circ}} = \sqrt{GM/R_{\text{vir}}}$ are computed. The wind speed and mass loading are then given by

$$v_w = \frac{(3 + \eta_0)}{\sqrt{2}} v_{\text{circ}}, \quad (6)$$

$$\eta = \frac{v_{\text{crit}}/v_{\text{circ}}}{\sqrt{2}}, \quad (7)$$

where $v_{\text{crit}} = 150 \text{ km s}^{-1}$ and $\eta_0 = 2$ (Oppenheimer & Davé 2008). In this model the effective value of ϵ_{SN} is no longer held constant, as the momentum carried by the wind is kept fixed instead. For galaxies in groups and clusters the wind energy exceeds that available from SNe. This is not necessarily a problem, as the winds may be driven by radiation pressure. However, for the parameter values of Oppenheimer & Davé (2008), the momentum that is injected also exceeds that available in the form of radiation (Haas et al., in preparation). These caveats should be kept in mind.

Figure 9 shows that model WVCIRC transports significantly more metals to low densities, strongly reducing the fraction of metals located up in high-metallicity stars, similar to WDENS (Fig. 8). However the temperature distribution of the metals in this model is quite different from that of WDENS with a much smaller fraction of metals at $\sim 10^6 \text{ K}$ and a much larger fraction at $\sim 10^5 \text{ K}$. WVCIRC predicts a metallicity of the diffuse IGM that is up to an order of magnitude higher than for the REFERENCE model. This is a consequence of the high mass loading factors used in small galaxies, which results in much more efficient transport from galaxies to the IGM, combined with the low wind velocities, which ensure that the winds do not shock the gas to high temperatures. The higher metallicity of the cold IGM agrees better with the observations, as was already shown by Oppenheimer & Davé (2006) for a similar model. Stellar metallicities, which are a factor of ≈ 2 lower by $z \approx 2$, also agree better with observations.

In Fig. 9 we also show results from another model, WThermal, discussed in Schaye et al. (2010) and Dalla Vecchia and Schaye (in prep.), in which the energy that is injected is again identical to that in the REFERENCE model, but in which this SN energy is deposited locally as *thermal* rather than kinetic energy. As star formation occurs in high density regions that cool efficiently, such a feedback mechanism may be very inefficient if the multi-phase nature of the ISM is not resolved (e.g. Katz 1992). Our implementation of thermal feedback avoids much of the overcooling problem by giving the energy to only a few particles so that they can be heated to sufficiently high temperatures that the cooling time is long (see also Theuns et al. 2002). Nevertheless, model WThermal predicts a greater fraction of metals to reside in dense gas and high-metallicity stars, indicating that the winds in this model are less efficient than in the REFERENCE model. The metallicity of the cold IGM is, however, higher, because of the lower temperature of the enriched gas, which is no longer shock-heated by high-velocity winds. Consequently, the metallicity of the WHIM is slightly lower for model WThermal.

⁵ Note that lowering v_0 , and thus increasing η_0 , would further boost the efficiency of the feedback in low-mass galaxies.

In summary, the details of the wind implementation have a large impact on the predicted metal census. In particular, the fraction of metals in a given phase varies strongly with the initial wind velocity and mass loading, even if the energy in the wind is kept fixed. Compared with the large range in metallicity spanned by the various phases, the effects of variations in the wind implementation on the metallicities are mostly minor. The metallicity of the cold IGM is most sensitive to wind implementation. While models with high wind velocities, and thus low mass loading factors, shift metals to lower densities, they tend to predict lower metallicities for the cold IGM, as the metals are shocked to high temperatures. Indeed, the high observed metallicities for this phase are better matched by models with low wind velocities. High wind velocities are, however, required for at least the more massive galaxies to reduce the stellar metallicities to the observed values. If we allow the wind parameters and energy to vary with the mass of the halo, with high mass loading factors in low-mass haloes and high wind velocities in high-mass haloes, then we can simultaneously boost the metallicity of the cold IGM and reduce that of the stars. This is the case for model WVCIRC (Oppenheimer & Davé 2008), although we noted that this model uses both more momentum and energy than is available from star formation. Finally, we note that it would be worthwhile to analyse the gas abundances in the simulations in a way that better mimics the observational determinations.

3.5 Active Galactic Nuclei

Feedback from accreting black holes in Active Galactic Nuclei (AGN) has for example been invoked to reproduce the observed black hole scaling relations, the break in the galaxy luminosity function, and the thermodynamic properties of groups and clusters of galaxies (e.g. Silk & Rees 1998; Kauffmann & Haehnelt 2000; Di Matteo et al. 2005; Bower et al. 2006; Croton et al. 2006; Booth & Schaye 2009, 2010; McCarthy et al. 2010).

Our models for black hole formation and the associated AGN feedback which are modified versions of the model of Springel et al. (2005) are fully described and tested in Booth & Schaye (2009) (see Schaye et al. 2010 for a comprehensive summary) and we therefore only touch on the details here. We seed low-mass haloes with central black holes, which are then allowed to grow by mergers and gas accretion. A fixed fraction of 1.5% of the accreted rest mass energy is injected into the ambient gas by heating it to a very high temperature. This model reproduces the Magorrian et al. (1998) relation, the normalisation of which is determined by the assumed efficiency factor of the feedback, as well as the other observed black hole scaling relations (Booth & Schaye 2009, 2010) and both the optical and X-ray properties of observed groups of galaxies (McCarthy et al. 2010).

Fig. 10 shows that AGN feedback is able to remove metals from high-density regions and transport them outside haloes (i.e., $\rho < 200 \langle \rho \rangle$), while heating them to high temperatures. The metallicity of the stars that contain most of the metals is reduced by nearly an order of magnitude. The metallicity evolution of the other phases is similar to the REFERENCE model, although the metallicity of the ICM is about a factor of two higher. Since there are less metals in the star-forming regions, it is not surprising that model AGN has lower stellar metallicities. However the WHIM's metallicity is also slightly reduced, notwithstanding the larger fraction of metals in the WHIM (as seen in the temperature PDF). AGN feedback (as implemented here) therefore increases the fraction of baryons in the WHIM.

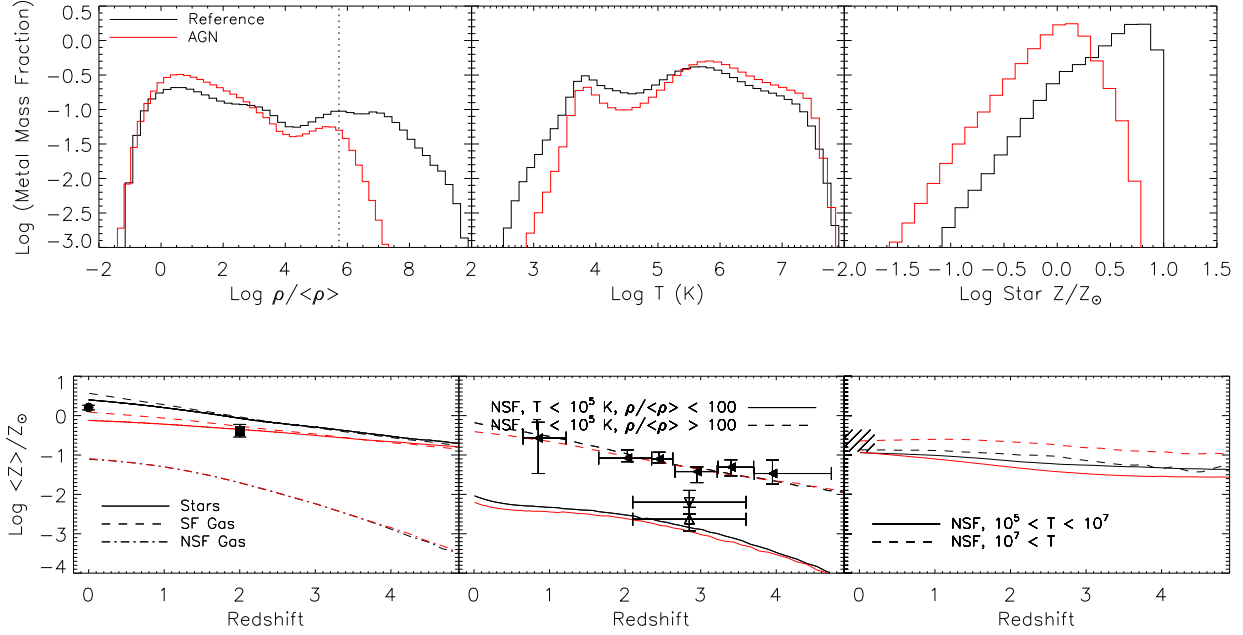


Figure 10. As Fig. 6, but for L100N512 simulations comparing the REFERENCE simulation (black) to model AGN (red), which includes feedback from accreting black holes. The metal mass weighted PDFs are for $z = 0$. AGN feedback is able to evacuate metals from the high-density regions and decreases the metallicity of stars at $z = 0$ by ≈ 0.5 dex. The metallicities of most of the other phases remain largely unchanged with the exception of the hottest phase whose metallicity increases by a about a factor of two.

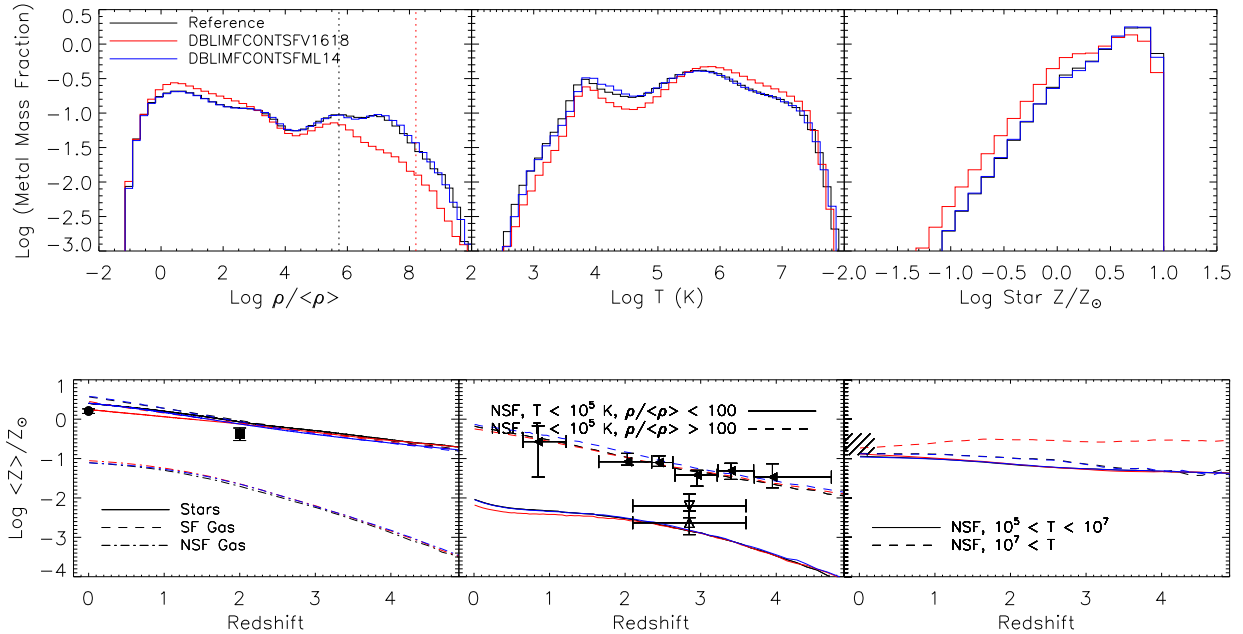


Figure 11. As Fig. 6, but for L100N512 simulations comparing the REFERENCE simulation (black), with two models with a top-heavy IMF at high-pressure; one in which the extra wind energy is used to increase the wind velocity ($v_w = 1618 \text{ km s}^{-1}$, DBLIMFCONTSFV1618, red), and one in which the extra wind energy is used to increase the mass loading ($\eta = 14$, DBLIMFCONTSFML14, blue). The metal mass weighted PDFs are for $z = 0$. In the top-left panel, the black and red dotted lines indicate the star formation threshold and the density above which the IMF becomes top-heavy, respectively. A top-heavy IMF in starbursts only makes a difference if the extra SN energy is used to increase the wind velocity, in which case it shifts metals to lower densities and higher densities and reduces the stellar metallicity.

3.6 A top-heavy IMF in starbursts

We now consider the effect of changing the IMF on the cosmic metal distribution. We will show that employing a top-heavy IMF in high-pressure regions affects mainly the stellar metallicity, leaving the metallicities of the other phases mostly unchanged. This is largely a result of the increased energy released from the SNe which are more prevalent for a top-heavy IMF.

There is tentative observational evidence that the IMF in some environments is ‘top-heavy’ as compared to the solar neighbourhood, such as in intense starbursts (McCradly et al. 2003, e.g.), or the inner parsec of the Galaxy (Maness et al. 2007, e.g.). Models of galaxy formation hint that such a top-heavy IMF may be required to explain galaxy counts in the submm and far IR (Lacey et al. 2008, e.g.). Padoan et al. (1997) and Larson (2005) discuss theoretical motivations for environmental dependence and evolution of the IMF, see Lacey et al. (2008) for more discussion.

We have implemented an environment-dependent IMF in our simulations, labelled DBLIMF in Table 1, in which the IMF is changed from the Chabrier fit to become top-heavy, $\Phi(M) \propto M^{-1}$ for all M (compared with $\Phi(M) \propto M^{-2.3}$ for $M > 1 M_{\odot}$ for Chabrier), above a density threshold of $n_{\text{H}} = 30 \text{ particles cm}^{-3}$, which corresponds to a pressure of $P/k = 2.0 \times 10^6 \text{ cm}^3 \text{ K}$. These values were chosen because they result in $\sim 10\%$ of the stellar mass forming with a top-heavy IMF. Because the star formation rate density increases with pressure, the IMF becomes top-heavy in regions with high star formation densities, i.e. ‘starbursts’. For the sake of brevity, we restrict ourselves to the case in which the star formation law is continuous across the ‘starburst’ pressure threshold (see Schaye et al. 2010 for a full discussion of this point; see section 3.7 for the results of models in which this is not the case). Note that these models are likely less well converged with respect to the numerical resolution than the REFERENCE model (see Schaye et al. 2010).

A top-heavy IMF increases the number of core-collapse SNe per unit stellar mass. We account for this by increasing the energy per unit stellar mass that is injected into the winds. We explore two extremes, one uses a higher mass-loading but the standard wind speed, ($\eta = 14, v_w = 600 \text{ km s}^{-1}$), the other uses the standard mass loading but higher wind speed, ($\eta = 2, v_w = 1618 \text{ km s}^{-1}$); note that this change is only enacted above the density threshold for top-heavy star formation.

In Fig. 11 we compare DBLIMFCONTSFV1618 ($\eta = 2, v_w = 1648 \text{ km s}^{-1}$) and DBLIMFCONTSFML14 ($\eta = 14, v_w = 600 \text{ km s}^{-1}$) with the REFERENCE model. While a top-heavy IMF increases the amount of metals produced per unit stellar mass in high-density regions due to the enhanced fraction of high-mass (high yield, short lifetime) stars, the increased feedback serves to move a lot of these metals to high temperatures and low densities, resulting in a slightly *lower* stellar metallicity, but a higher ICM metallicity for DBLIMFCONTSFV1618. Channeling the extra feedback energy into a higher mass loading factor yields metallicities and metal mass distributions that are nearly identical to those of the REFERENCE model. This is because feedback in high-pressure gas is inefficient for such a low wind velocity.

The use of a top-heavy IMF in ‘starbursts’, as implemented in the DBLIMF models, has surprisingly little effect on the relative abundance of α -enriched elements produced by these massive stars (not plotted). While $[\text{O}/\text{Fe}]$ averaged over entire simulation volume is higher for a top-heavy IMF, the diffuse IGM and cold halo gas have a *lower* α enhancement if the IMF is top heavy, because the α elements are deposited in hotter gas. This confirms that the dif-

ferences between the REFERENCE model and the top-heavy IMF in starbursts models are driven by the changes in the feedback rather than by the increased metal production.

3.7 Other models

Although some processes can dramatically affect the cosmic metal distribution, we will see in Figs. 12–15 that there are a number of models that show little difference. It is remarkable that many drastic changes in physical parameters and processes have little effect on the metallicity and metal mass distribution of most, or even all, phases. We briefly comment on each of the models that exhibit this behaviour and refer to Schaye et al. (2010) for more detailed descriptions of the models.

NOREION, REIONZ06, REIONZ12 - We have also varied the reionization history of hydrogen in our simulations. Whereas the REFERENCE model assume H reionization at $z_r = 9$, these models have no reionization, $z_r = 6$ and 12, respectively. We find that so long as the heating from reionization happens, the simulations have a very ‘short’ memory of their thermal history. If there is no heating from reionization, then a slightly larger fraction of the metals lie in cold gas, although the metallicity of cold, dense gas is actually a little lower.

Aside from directly heating the mass, the reionization history determines the lowest halo mass in which galaxies are able to form. This may be especially important since Wiersma et al. (2010) and Booth et al. (2010) showed that the diffuse IGM is typically enriched by low-mass haloes at high redshift. Between $z = 9$ and $z = 0$, the virial mass of corresponding to 10^4 K increases from $\approx 2 \times 10^8 M_{\odot}$ to $\approx 3 \times 10^9 M_{\odot}$. Even the latter corresponds to only $\approx 3 \times 10^2$ dark matter particles in our $25h^{-1} \text{ Mpc}$ box. It is therefore likely that we have strongly underestimated the importance of the reionisation history for the metal content of the IGM.

SFAMPLx3, SFSLOPE1p75, SFTHRESZ - The normalisation, power-law index, and threshold gas density of the Kennicutt-Schmidt star formation law (Eq. 2) are varied. The first model assumes a normalisation that is higher by a factor of 3; the second model has a slope of 1.75 (as opposed to 1.4); in the last model the threshold for star formation decreases with increasing metallicity. For models with more efficient star formation, the fraction of the metals residing in the ISM is lower. This is because feedback allows star formation to self-regulate, such that the rate of energy injection is independent of the star formation law. Hence, a shorter gas consumption time scale is balanced by the ejection of gas (and metals) from galaxies, such that the star formation rate remains the same (Schaye et al. 2010). As the ISM has a higher metallicity than the gas at larger distances, this transfer of metals increases the metallicity of cold, halo gas, while leaving the metallicity of the ISM unchanged.

NOAGB_NOSNIa - The contribution from AGB and type Ia SNe to stellar mass loss and feedback is ignored. Schaye et al. (2010) showed that this change reduces the $z = 0$ star formation rate by about 40%. We find that the metallicities drop by a similar factor, but that the metal mass fractions remain essentially unchanged. The abundance ratios (not shown) evolve very little and reflect solely the SNII yields ($[\text{O}/\text{Fe}] \approx 0.7$ for all redshifts and phases).

EOS1p0, EOS1p67 - The slope, γ_{eff} , of the $p \propto \rho_{\text{eff}}^{\gamma_{\text{eff}}}$ relation imposed on star-forming gas, is changed from the value $\gamma_{\text{eff}} = 4/3$ assumed in the REFERENCE model to 1 and 5/3, respectively. As was the case for the cosmic star formation history (Schaye et al.

2010), this change has no significant effect on the metal distribution.

IMFSALP - Assumes a Salpeter IMF, as opposed to the Chabrier IMF. The change in IMF results in a small (less than a factor of two) decrease in the metallicities and [O/Fe] ratios (not plotted) of all phases, which reflects the lower rate of metal production per unit stellar mass and the lower star formation rates that result from the associated reduction in the cooling rates (see Schaye et al. 2010).

WHYDRODEC - Wind particles are temporarily ‘decoupled’ from the hydrodynamics (i.e. they feel only gravity) as in the widely used model of Springel & Hernquist (2003). This modification has a significant effect, decreasing the metallicities of stars and the cold IGM by about a factor of two. Moreover, it roughly doubles the fraction of metals in, but not the metallicity of, the WHIM at the expense of the fraction locked up in stars. We have relegated this simulation to this overview due to space constraints, but it is an important variation.

MILL - This model use the cosmological parameters of the Millennium simulation (Springel 2005), as opposed to the WMAP3 values. The most significant difference is the larger value of σ_8 in the MILL model (0.9 vs. 0.74), which implies that structure forms slightly earlier. The wind mass loading is doubled ($\eta = 4$, $v_w = 600 \text{ km s}^{-1}$) in order to retain the match to the peak of the cosmic star formation history (Schaye et al. 2010). Compared with the REFERENCE model, all of the curves shift to higher redshifts, but as Figs. 12–15 show, even such a large change in cosmology has only a minor effect on the predictions for $z = 0$ and 2.

DBLMFML14, DBLMFV1618 - These models assume a top-heavy IMF for stars formed in high-pressure regions. They are identical to the models we discussed in section 3.6, except that the star formation law is discontinuous across the ‘starburst’ threshold. Since no discontinuities in star formation density (as a function of gas density) have been observed, this model decreases the efficiency of star formation in high-pressure regions in order to produce a continuous UV flux as a function of pressure. The fact that these models show little difference to their DBLMFCONTSF counterparts is consistent with our finding that variations in the star formation law are unimportant.

NOHeHEAT - As discussed in section 2, we include some heating around $z \approx 3$ to account for the rise in the IGM temperature around the time of helium reionization. Ignoring this extra heat input does not yield any significant differences, as was also true for the cosmic star formation history (Schaye et al. 2010).

SNiGAUSS - Given the large uncertainties in the normalisation and shape of the cosmic SNIa rate, we have run a model where it is based on a Gaussian delay function (rather than the e-folding delay function used in the REFERENCE model). This results in roughly the same number of SNIa, but they happen much later in the history of the universe. The evolution of the [O/Fe] ratio shows the expected differences (the dip to lower values occurring at lower redshift), but the overall distribution of metals and metallicity are nearly identical to the results for the REFERENCE model.

3.8 Summary

Figures 12 – 15 summarise our different models, comparing metal fractions and metallicities at redshifts $z = 0$ for the $100h^{-1}$ Mpc and at $z = 2$ for the $25h^{-1}$ Mpc simulations. Note that many models were only run in one of the two boxes (see Table 1). We give observational estimates of metallicities to compare to, but we cau-

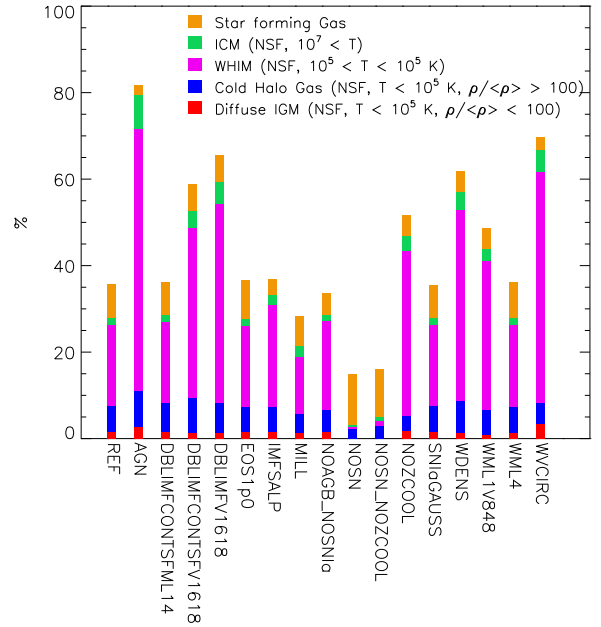


Figure 12. Fraction of metal mass in various phases for a selection of L100N512 models of the OWLS suite at $z = 0$. The orange, green, magenta, blue and red bars correspond to the metal mass fraction in star-forming gas, ICM, WHIM, cold halo gas, and diffuse IGM, respectively. The remainder of metals is locked up in stars. Metal fractions depend largely on the strength of feedback - models without feedback have very high stellar metal fractions, whereas models with strong feedback predict that most metals reside in the WHIM.

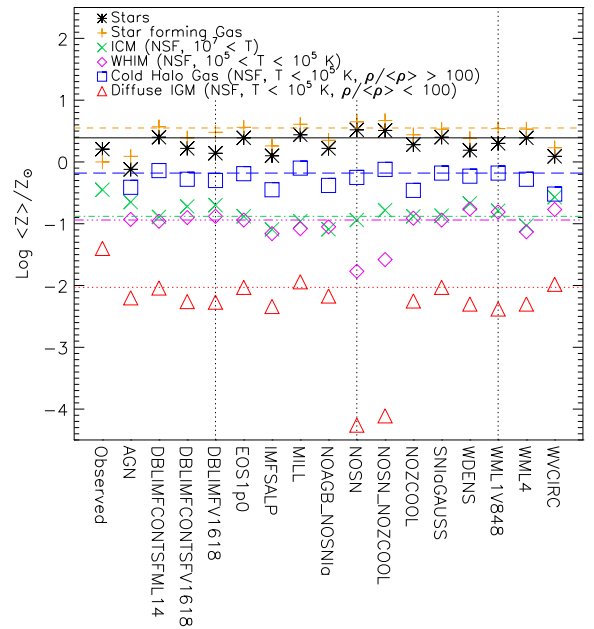


Figure 13. Metallicities of various phases for a selection of L100N512 models of the OWLS suite at $z = 0$. The values for the REFERENCE model are indicated by the horizontal lines. Observations shown are as follows: stars - Gallazzi et al. (2008); ICM - Simionescu et al. (2009); the rest - estimates compiled by Pagel (2008). The metallicities are surprisingly similar across most models, but models without feedback are clearly different.

two components. Fast galactic winds in massive galaxies, e.g. resulting from a top-heavy IMF at high gas pressures, work in the same direction but have a smaller effect than AGN. Efficient feedback in high-mass galaxies only has a relatively small effect on the metallicities of the diffuse gas components.

- Changes in the star formation law, the structure of the ISM, the cosmology, and the IMF all play a role, but are less important than the inclusion and implementation of metal-line cooling and, most importantly, outflows driven by feedback from star formation and accreting supermassive black holes. We also find a small effect for changes in the reionisation history, but for the case of the IGM this may be due to our limited resolution.

We summarise the metal mass distribution as follows:

- Stars and the WHIM are the dominant depositories of metals. In all models they contain together at least 78 % of the metals at $z = 0$ and at least 53 % at $z = 2$. At high redshift the ISM also contains a large fraction of the metals: at least 11 % in all simulations at $z = 2$. In all our models, and at both $z = 0$ and $z = 2$, the remaining components (diffuse cold-warm IGM, cold halo gas, and ICM) together contain less than a quarter of the metals.

- The mean metallicities of the WHIM and ICM are nearly constant in time. In most models they increase slightly with time to $\sim 10^{-1} Z_{\odot}$ at $z = 0$. In contrast, the metallicities of the cold halo gas and the diffuse IGM, increase by more than an order of magnitude from $z = 5$ to 0.

- All our models predict, both for $z = 0$ and 2, mean metallicities of $Z \sim Z_{\odot}$ for stars and ISM, and $10^{-1} Z_{\odot} \lesssim Z < Z_{\odot}$ for the ICM and for cold halo gas. Except for the models without SN feedback, all simulations predict, both for $z = 0$ and 2, mean metallicities of $Z \sim 10^{-1} Z_{\odot}$ for the WHIM and $10^{-3} Z_{\odot} \lesssim Z \lesssim 10^{-2} Z_{\odot}$ for the diffuse cold-warm IGM.

The inclusion and implementation of outflows driven by feedback from star formation and AGN is most important for predictions of the distribution of metals. As cosmological simulations will need to continue to use sub-grid implementations for these processes for the foreseeable future, this implies that predicting the distribution of metals will remain difficult for ab initio models. However, as we have shown, provided that some feedback is included, the mean metallicities of most different components can be robustly predicted to order of magnitude.

The sensitivity of some of the results to feedback can also be regarded as fortunate. It gives us a useful tool to study the effects of outflows, which are an essential but very poorly understood ingredient of models of galaxy formation and evolution. The metallicity of the diffuse warm-cold IGM, which can be constrained using QSO absorption lines, is particularly sensitive to variations in the models and is therefore a very promising probe of the physics of galactic outflows.

ACKNOWLEDGMENTS

It is a great pleasure to thank all the members of the OWLS team for discussions and help. The simulations presented here were run on Stella, the LOFAR BlueGene/L system in Groningen, on the Cosmology Machine at the Institute for Computational Cosmology in Durham as part of the Virgo Consortium research programme, and on Darwin in Cambridge. This work was sponsored by the National Computing Facilities Foundation (NCF) for the use of supercomputer facilities, with financial support from the Netherlands Orga-

nization for Scientific Research (NWO), also through a VIDI grant. This work was also supported by DFG Priority Program 1177.

REFERENCES

- Aguirre A., Dow-Hygelund C., Schaye J., Theuns T., 2008, *ApJ*, 689, 851
- Aguirre A., Hernquist L., Schaye J., Katz N., Weinberg D. H., Gardner J., 2001, *ApJ*, 561, 521
- Aguirre A., Hernquist L., Schaye J., Weinberg D. H., Katz N., Gardner J., 2001, *ApJ*, 560, 599
- Ando M., Ohta K., Iwata I., Akiyama M., Aoki K., Tamura N., 2007, *PASJ*, 59, 717
- Bekki K., Chiba M., 2009, *PASA*, 26, 48
- Berczik P., 1999, *A&A*, 348, 371
- Booth C. M., Schaye J., 2009, *MNRAS*, 398, 53
- Booth C. M., Schaye J., 2010, *MNRAS*, 405, L1
- Booth C. M., Schaye J., Delgado J. D., Dalla Vecchia C., 2010, *arXiv:1011.5502*
- Bouché N., Lehnert M. D., Aguirre A., Péroux C., Bergeron J., 2007, *MNRAS*, 378, 525
- Bower R. G., Benson A. J., Malbon R., Helly J. C., Frenk C. S., Baugh C. M., Cole S., Lacey C. G., 2006, *MNRAS*, 370, 645
- Brook C. B., Kawata D., Scannapieco E., Martel H., Gibson B. K., 2007, *ApJ*, 661, 10
- Cen R., Ostriker J. P., 1999, *ApJ*, 519, L109
- Cen R., Ostriker J. P., 2006, *ApJ*, 650, 560
- Chabrier G., 2003, *PASP*, 115, 763
- Churchill C. W., Kacprzak G. G., Steidel C. C., Evans J. L., 2007, *ApJ*, 661, 714
- Cowie L. L., Songaila A., 1998, *Nature*, 394, 44
- Crain R. A., Theuns T., Dalla Vecchia C., et al., 2009, *MNRAS*, 399, 1773
- Croton D. J., Springel V., White S. D. M., De Lucia G., Frenk C. S., Gao L., Jenkins A., Kauffmann G., Navarro J. F., Yoshida N., 2006, *MNRAS*, 365, 11
- Dalla Vecchia C., Schaye J., 2008, *MNRAS*, 387, 1431
- de Plaa J., Werner N., Bykov A. M., et al., 2006, *A&A*, 452, 397
- Di Matteo T., Springel V., Hernquist L., 2005, *Nature*, 433, 604
- Dunne L., Eales S. A., Edmunds M. G., 2003, *MNRAS*, 341, 589
- Ellison S. L., Songaila A., Schaye J., Pettini M., 2000, *AJ*, 120, 1175
- Erb D. K., Shapley A. E., Pettini M., Steidel C. C., Reddy N. A., Adelberger K. L., 2006, *ApJ*, 644, 813
- Fabjan D., Borgani S., Tornatore L., Saro A., Murante G., Dolag K., 2010, *MNRAS*, 401, 1670
- Ferland G. J., Korista K. T., Verner D. A., Ferguson J. W., Kingdon J. B., Verner E. M., 1998, *PASP*, 110, 761
- Fukugita M., Hogan C. J., Peebles P. J. E., 1998, *ApJ*, 503, 518
- Gallazzi A., Brinchmann J., Charlot S., White S. D. M., 2008, *MNRAS*, 383, 1439
- Gnedin N. Y., 1998, *MNRAS*, 294, 407
- Governato F., Willman B., Mayer L., Brooks A., Stinson G., Valenzuela O., Wadsley J., Quinn T., 2007, *MNRAS*, 374, 1479
- Haardt F., Madau P., 2001, in Neumann D. M., Tran J. T. V., eds, *Clusters of Galaxies and the High Redshift Universe Observed in X-rays Modelling the UV/X-ray cosmic background with CUBA*
- Halliday C., Daddi E., Cimatti A., et al., 2008, *A&A*, 479, 417
- Jarosik N., Bennett C. L., Dunkley J., et al., 2010, *ArXiv e-prints*
- Katz N., 1992, *ApJ*, 391, 502
- Kauffmann G., Haehnelt M., 2000, *MNRAS*, 311, 576

- Kawata D., 2001, *ApJ*, 558, 598
- Kawata D., Gibson B. K., 2003, *MNRAS*, 346, 135
- Kennicutt Jr. R. C., 1998, *ApJ*, 498, 541
- Kobayashi C., 2004, *MNRAS*, 347, 740
- Kobayashi C., Springel V., White S. D. M., 2007, *MNRAS*, 376, 1465
- Kobulnicky H. A., Zaritsky D., 1999, *ApJ*, 511, 118
- Kunth D., Östlin G., 2000, *ARA&A*, 10, 1
- Lacey C. G., Baugh C. M., Frenk C. S., Silva L., Granato G. L., Bressan A., 2008, *MNRAS*, 385, 1155
- Larson R. B., 2005, *MNRAS*, 359, 211
- Leccardi A., Molendi S., 2008, *A&A*, 487, 461
- Lia C., Portinari L., Carraro G., 2002, *MNRAS*, 330, 821
- Magorrian J., Tremaine S., Richstone D., et al., 1998, *AJ*, 115, 2285
- Maness H., Martins F., Trippe S., et al., 2007, *ApJ*, 669, 1024
- Mannucci F., Cresci G., Maiolino R., et al., 2009, *MNRAS*, 398, 1915
- Marigo P., 2001, *A&A*, 370, 194
- Maughan B. J., Jones C., Forman W., Van Speybroeck L., 2008, *ApJS*, 174, 117
- McCarthy I. G., Schaye J., Ponman T. J., et al., 2010, *MNRAS*, 406, 822
- McCraday N., Gilbert A. M., Graham J. R., 2003, *ApJ*, 596, 240
- Meiring J. D., Lauroesch J. T., Kulkarni V. P., Péroux C., Khare P., York D. G., 2009, *MNRAS*, 397, 2037
- Mori M., Umemura M., 2006, *Nature*, 440, 644
- Mosconi M. B., Tissera P. B., Lambas D. G., Cora S. A., 2001, *MNRAS*, 325, 34
- Mushotzky R., Loewenstein M., Arnaud K. A., Tamura T., Fukazawa Y., Matsushita K., Kikuchi K., Hatsukade I., 1996, *ApJ*, 466, 686
- Oppenheimer B. D., Davé R., 2006, *MNRAS*, 373, 1265
- Oppenheimer B. D., Davé R., 2008, *MNRAS*, 387, 577
- Padoan P., Nordlund A., Jones B. J. T., 1997, *MNRAS*, 288, 145
- Pagel B. E. J., 2008, in Knapen J. H., Mahoney T. J., Vazdekis A., eds, *Pathways Through an Eclectic Universe Vol. 390 of Astrophysical Society of the Pacific Conference Series, Where Are the Missing Baryons and Metals?*, pp 483–+
- Pasetto S., Grebel E. K., Berczik P., Spurzem R., Dehnen W., 2010, *A&A*, 514, A47+
- Pettini M., Smith L. J., Hunstead R. W., King D. L., 1994, *ApJ*, 426, 79
- Portinari L., Chiosi C., Bressan A., 1998, *A&A*, 334, 505
- Price P. A., Songaila A., Cowie L. L., Bell Burnell J., Berger E., Cucchiara A., Fox D. B., Hook I., Kulkarni S. R., Penprase B., Roth K. C., Schmidt B., 2007, *ApJ*, 663, L57
- Prochaska J. X., Gawiser E., Wolfe A. M., Castro S., Djorgovski S. G., 2003, *ApJL*, 595, L9
- Rahimi A., Kawata D., Brook C. B., Gibson B. K., 2010, *MNRAS*, 401, 1826
- Raiteri C. M., Villata M., Navarro J. F., 1996, *A&A*, 315, 105
- Rasmussen J., Ponman T. J., 2007, *MNRAS*, 380, 1554
- Recchi S., Matteucci F., D’Ercole A., 2001, *MNRAS*, 322, 800
- Romeo A. D., Sommer-Larsen J., Portinari L., Antonuccio-Delogu V., 2006, *MNRAS*, 371, 548
- Sato K., Tokoi K., Matsushita K., Ishisaki Y., Yamasaki N. Y., Ishida M., Ohashi T., 2007, *ApJL*, 667, L41
- Scannapieco C., Tissera P. B., White S. D. M., Springel V., 2005, *MNRAS*, 364, 552
- Scannapieco E., Pichon C., Aracil B., Petitjean P., Thacker R. J., Pogosyan D., Bergeron J., Couchman H. M. P., 2006, *MNRAS*, 365, 615
- Schaye J., 2004, *ApJ*, 609, 667
- Schaye J., Aguirre A., Kim T.-S., Theuns T., Rauch M., Sargent W. L. W., 2003, *ApJ*, 596, 768
- Schaye J., Carswell R. F., Kim T., 2007, *MNRAS*, 379, 1169
- Schaye J., Dalla Vecchia C., 2008, *MNRAS*, 383, 1210
- Schaye J., Dalla Vecchia C., Booth C. M., et al., 2010, *MNRAS*, 402, 1536
- Schaye J., Rauch M., Sargent W. L. W., Kim T. S., 2000, *ApJ*, 541, L1
- Seljak U., Zaldarriaga M., 1996, *ApJ*, 469, 437
- Shen S., Wadsley J., Stinson G., 2009, *ArXiv e-prints*
- Silk J., Rees M. J., 1998, *A&A*, 331, L1
- Simcoe R. A., Sargent W. L. W., Rauch M., 2004, *ApJ*, 606, 92
- Simionescu A., Werner N., Böhringer H., Kaastra J. S., Finoguenov A., Brüggén M., Nulsen P. E. J., 2009, *A&A*, 493, 409
- Snowden S. L., Mushotzky R. F., Kuntz K. D., Davis D. S., 2008, *A&A*, 478, 615
- Sommer-Larsen J., Fynbo J. P. U., 2008, *MNRAS*, 385, 3
- Sommer-Larsen J., Romeo A. D., Portinari L., 2005, *MNRAS*, 357, 478
- Songaila A., Cowie L. L., 1996, *AJ*, 112, 335
- Springel V., 2005, *MNRAS*, 364, 1105
- Springel V., Di Matteo T., Hernquist L., 2005, *MNRAS*, 361, 776
- Springel V., Hernquist L., 2003, *MNRAS*, 339, 289
- Steinmetz M., Müller E., 1995, *MNRAS*, 276, 549
- Stinson G., Seth A., Katz N., Wadsley J., Governato F., Quinn T., 2006, *MNRAS*, 373, 1074
- Theis C., Burkert A., Hensler G., 1992, *A&A*, 265, 465
- Theuns T., Viel M., Kay S., Schaye J., Carswell R. F., Tzanavaris P., 2002, *ApJ*, 578, L5
- Thielemann F.-K., Argast D., Brachwitz F., et al., 2003, in *From Twilight to Highlight: The Physics of Supernovae Supernova Nucleosynthesis and Galactic Evolution*, pp 331–+
- Tornatore L., Borgani S., Dolag K., Matteucci F., 2007, *MNRAS*, 382, 1050
- Tornatore L., Borgani S., Matteucci F., Recchi S., Tozzi P., 2004, *MNRAS*, 349, L19
- Tornatore L., Borgani S., Viel M., Springel V., 2009, *ArXiv e-prints*
- Tremonti C. A., Heckman T. M., Kauffmann G., et al., 2004, *ApJ*, 613, 898
- Valdarnini R., 2003, *MNRAS*, 339, 1117
- Wiersma R. P. C., Schaye J., Dalla Vecchia C., Booth C. M., Theuns T., Aguirre A., 2010, *MNRAS*, 409, 132
- Wiersma R. P. C., Schaye J., Smith B. D., 2009, *MNRAS*, 393, 99
- Wiersma R. P. C., Schaye J., Theuns T., Dalla Vecchia C., Tornatore L., 2009, *MNRAS*, 399, 574